Simulations of submonolayer Xe on Pt(111): The case for a chaotic low temperature phase

Anthony D. Novaco, and Jessica Bavaresco

Citation: The Journal of Chemical Physics **148**, 144704 (2018); doi: 10.1063/1.5024027
View online: https://doi.org/10.1063/1.5024027
View Table of Contents: http://aip.scitation.org/toc/jcp/148/14
Published by the American Institute of Physics

Simulations of submonolayer Xe on Pt(111): The case for a chaotic low temperature phase

Anthony D. Novaco[1,a)] and Jessica Bavaresco[2,b)]
[1]*Department of Physics, Lafayette College, Easton, Pennsylvania 18042, USA*
[2]*Institute for Quantum Optics and Quantum Information (IQOQI), Austrian Academy of Sciences, Boltzmanngasse 3, A-1090 Vienna, Austria*

(Received 30 January 2018; accepted 22 March 2018; published online 10 April 2018)

Molecular dynamics simulations are reported for the structural and thermodynamic properties of submonolayer xenon adsorbed on the (111) surface of platinum for temperatures up to the (apparently incipient) triple point and beyond. While the motion of the atoms in the surface plane is treated with a standard two-dimensional molecular dynamics simulation, the model takes into consideration the thermal excitation of quantum states associated with surface-normal dynamics in an attempt to describe the apparent smoothing of the corrugation with increasing temperature. We examine the importance of this thermal smoothing to the relative stability of several observed and proposed low-temperature structures. Structure factor calculations are compared to experimental results in an attempt to determine the low temperature structure of this system. These calculations provide strong evidence that, at very low temperatures, the domain wall structure of a xenon monolayer adsorbed on a Pt(111) substrate possesses a chaotic-like nature, exhibiting long-lived meta-stable states with pinned domain walls, these walls having narrow widths and irregular shapes. This result is contrary to the standard wisdom regarding this system, namely, that the very low temperature phase of this system is a striped incommensurate phase. We present the case for further experimental investigation of this and similar systems as possible examples of chaotic low temperature phases in two dimensions. *Published by AIP Publishing.* https://doi.org/10.1063/1.5024027

I. INTRODUCTION

The physical adsorption of gas atoms (adatoms) on solid crystalline substrates produces an interesting collection of phase transitions in a nearly two-dimensional (2D) environment.[1] These include a rich variety of structural phase transitions driven by mismatches between the natural periodicities of the adsorbed layer and the crystalline substrate.[2,3] These effects are not restricted to the lowest layer, but can be found even in upper layers as they are subjected to the periodic field generated by the lower ones.[3–5]

Of the various possible combinations of adsorbates and adsorbents, the adsorption of noble gas atoms on well-ordered crystalline surfaces provides an especially attractive and useful set of examples for both theorists and experimentalists interested in fundamental questions.[6] There are a number of reasons to consider these excellent examples of model systems. First, the interactions between the various noble gas atoms in a vacuum are simple and well understood[7] with the modifications to these interactions due to the adsorption of the atoms on certain surfaces being reasonably well modeled.[8] Second, there is a well-developed approach to the interaction of these atoms with the crystalline surfaces[9] with the values of the interaction parameters (for many specific systems) being reasonably well determined.[10] Therefore, there is the opportunity to make quantitative comparisons between theory and experiment with some confidence, more than may be justified for many other adsorbate-adsorbent combinations (where the modeling is not on as firm a foundation and the systems are not as well characterized).[11–13]

The adsorption of a xenon adatom on the (111) surface of platinum (Xe/Pt) is one of the more interesting cases of physical adsorption.[14–16] Unlike many of the cases involving the physical adsorption of noble gas atoms on crystalline substrates, the sites for adsorption are directly "over" the Pt surface atoms and not at the hollow positions,[16,17] the latter being the expected situation for dielectric surfaces and confirmed for Xe on the basal plane surface of graphite (Xe/Gr). Perhaps related to this, the corrugation along the surface plane is much larger than it is for many other cases of the adsorption of noble gases.[18] This strong bonding of the xenon adatom to the platinum surface is associated with a significant redistribution of the electron density in both the adatom and the platinum surface atoms, which gives this system some characteristics of chemisorption.[19]

The strong corrugation and dilated lattice of Xe/Pt suggests an interesting question: Is there anything unusual about the structure of this system at very low temperatures? In chemisorbed systems, there exist examples exhibiting chaotic structures at very low temperatures.[20] Paradoxically, at higher temperatures, such systems relax to form a more regular, ordered structure. Similar behavior has been seen in some magnetic systems[21] and in systems with charge-density waves.[22] In all these cases, the resulting chaotic structure can be attributed to pinned domain walls which lock down the structure with a

[a)]E-mail: novacoad@lafayette.edu
[b)]E-mail: jessica.bavaresco@oeaw.ac.at

certain degree of randomness in the placement of these walls.[22] In adsorbed systems, this chaotic behavior relies on the forces of the substrate lattice acting on the domain walls (the Peierls pinning force)[21–27] being comparable to or stronger than the interactions between these domain walls.[22] This same physics appears to be important to a related problem, the development of friction in monolayer patches sliding across periodic substrates.[28–30]

Here we investigate whether similar chaotic behavior at low-temperatures can be present in the physical adsorption case of Xe/Pt. In order to do so, we perform molecular dynamics (MD) simulations using a hybrid approach, combining a classical treatment of the dynamics along the surface with a quantum treatment of the dynamics perpendicular to that surface. We refer to this as a quasi-two-dimensional (Q2D) treatment, justifying this treatment based upon the very different nature of the variation in the surface interaction along the surface compared to the variation perpendicular to that surface. Our model is constructed using a combination of the Barker-Rettner (BR) model[18] for Xe/Pt with a Xe–Xe "Hartree-Fock-Dispersion" (HFD) interaction,[7] modified by the McLachlan interaction for Xe/Pt.[31] The largest case study reported here approaches the size of some experimental systems but is smaller than the experimental best-case scenario.[32,33]

We provide evidence of irregular, extremely narrow domain walls for the low-temperature Xe/Pt system. These walls tend to zigzag in a rather haphazard (and perhaps "chaotic") fashion and do not appear to relax as the run is extended in time, nor when the temperature is raised. This behavior is consistent with these domain walls being pinned, at low temperature, by the Peierls force and is in agreement with early preliminary calculations.[34] We will label such structures as chaotic, although we cannot show that they fit any strict definition of such a state. We will use the phrase "disordered state" to refer to the phase above the melting transition.[35]

We also report other structural and thermodynamic analyses for constrained (the xenon monolayer uniformly fills the entire simulation cell) and unconstrained (a xenon patch in the center of the simulation cell) system geometries. This includes calculations of substrate corrugation parameters, determination of the ground state phase, and evidence of meta-stability for the low temperature phases. The effects of size dependence are made explicit by the calculation of both ψ_0 (the hexatic order parameter)[36] and ψ_6 (the net-domain-phase order parameter)[35] as functions of the temperature and size of the system. The effects of the rotation of the monolayer with respect to the substrate are also examined. Some of these results are to be found in the supplementary material.

Our calculations of the static structure factor allow for comparisons between our simulations and the known experimental results. There is a claim, based upon helium atom scattering (HAS) experiments,[37] that the very low temperature phase of Xe/Pt is a striped incommensurate (SIC) phase. This has become the conventional wisdom for this system.[2,38] The principle experimental evidence for this striped phase involves an analysis of the static structure factor, comparing the hexagonal domain wall structure to that of the striped phase.[32,39–41] However, it does appear that this analysis did not consider the possibility of a chaotic (i.e., disorganized) domain structure that is made evident in our simulations and, as such, makes no prediction about the existence of such a state.

We show that chaotic-like structures can exist as meta-stable (long-lived) states in Xe/Pt. Furthermore, the resulting structures can mimic the experimental results used as evidence for the striped phase. In addition, some aspects of the experimental results seem at odds with the structure factor for the meta-stable striped phase reported here. Some results of our simulations have been reported in Ref. 35; this article is both a follow-up to and a completion of that work.

II. MODEL FOR Xe ADSORBED ON Pt(111)

Much of the behavior seen in the simulations of this system is driven by the strong corrugation and the dilated lattice of Xe/Pt. The minimum barrier to translation from one adsorption site to the next is roughly 275 K, whereas the minimum in the effective interaction between xenon atoms is about 238 K.[42] By contrast, the minimum barrier to translation for Xe/Gr is about 50 K, while the Xe–Xe interaction is nearly unchanged.[36,43] In addition, the Xe–Xe spacing for the $\sqrt{3} \times \sqrt{3}$ R 30° ($\sqrt{3}$) phase of Xe/Pt is 4.80 Å which is significantly larger than the position of the minimum in the Xe-Xe interaction (4.37 Å). It would seem that this particular combination of a large corrugation and a dilated $\sqrt{3}$ lattice is what leads to a replacement of a normal triple-point transition with an order-disorder transition (an incipient triple-point).[35] We did not explore the boundaries of the parameter space that would generate this behavior.

The literature for classical simulations of the Xe/Pt monolayer, both Molecular Dynamics (MD) and Monte Carlo (MC), is quite sparse. There are some early MD simulations of small systems,[44–48] but no MC work to speak of. There is an extensive body of work (by Bruch and Gottlieb) on the stability of various possible structures that might exist in this sort of system (using a harmonic lattice dynamics approach). In particular, there is a direct application of their ideas to the Xe/Pt system,[49–51] Unfortunately, some of these early calculations used older (and less realistic) forms for the Xe–Xe interactions and/or simplistic models for the Xe–Pt interactions. However, the stability of the various possible structures for this system has been shown to be sensitive to relatively small changes in these interactions.[35,48,49]

A model that has been successful in describing the interaction of a xenon atom with the platinum (111) surface is that of Barker and Rettner (BR),[18] a semi-empirical model that fits a significant collection of experimental data. Only a few of the early calculations for Xe/Pt used the BR model for this interaction, and more importantly, these calculations did not directly examine the effects of thermal excitation perpendicular to the surface on the effective corrugation of the system. This motion has an important effect on the thermal smoothing of the corrugation and thus on the thermal properties of the monolayer.[35] Furthermore, when the dynamics of this and other adsorbed systems in the surface-normal direction has been treated, it has typically been done by using a purely classical treatment of that motion.[48,52–55]

The problem with a purely classical approach to the surface-normal dynamics is that even when the surface-parallel motion is well treated by classical dynamics, the same cannot be said of the surface-normal dynamics. This is due to the narrowness of the potential energy well in the surface-normal direction and the corresponding large excitation energies of the adatom. The corresponding thermal motion has an important influence on the effective corrugation and thus on the predictions of stable structures and phase transitions in this system.[27,35,48] In the following, we describe how our model is constructed to overcome these issues.

A. Q2D approach

The adatom coordinates along the surface plane are (x, y) (denoted by $\boldsymbol{r}$), while the coordinate in the surface-normal direction is z. We start with a quantum description of the system, approximating the exact wave function by a set of product wave functions having the form[56]

$$\Psi(\boldsymbol{r}_1, z_1, \boldsymbol{r}_2, z_2, \ldots) = \Psi_{\parallel}(\boldsymbol{r}_1, \boldsymbol{r}_2, \ldots) \times \Psi_{\perp}(z_1, z_2, \ldots). \quad (1)$$

More to the point, we consider the Hilbert space of all such functions, assuming appropriate orthogonality and completeness conditions for the set. It must be noted that, in the end, we will approximate the dynamics of the surface parallel terms using a classical MD simulation but will retain a quantum description of the surface-normal dynamics as noted in the previous paragraph.

Following Ref. 56, it is convenient to consider three subsets of contributions to the total energy of the system. These three energy contributions are denoted by E_z, E_{xy}, and E_{xyz} (each on a per adatom basis). The first contribution, E_z, is the kinetic energy associated with the z-direction plus the laterally averaged substrate interaction $U_0(z)$. This term depends only on the $\Psi_{\perp}$ factor, and it is the thermal behavior of this factor that is primarily responsible for the temperature dependence of the substrate corrugation. The second contribution, E_{xy}, is the remaining kinetic energy terms plus the interaction between the xenon adatoms. Strictly speaking, this interaction term depends upon both the $\boldsymbol{r}$ and z variations of the wave function. However, it is a very good approximation to treat this as dependent only on the $\Psi_{\parallel}$ factor because of the narrowness of the $\Psi_{\perp}$ functions.[56] The third and final term consists of the remaining contributions to the Xe/Pt interaction, that is, the non-zero $\boldsymbol{G}$ (platinum reciprocal lattice vectors) terms in a Fourier expansion of the BR interaction, projected onto the $\boldsymbol{r}$ plane as described below and in the supplementary material. This term, which determines the effective corrugation, depends on both the $\Psi_{\parallel}$ and the $\Psi_{\perp}$ factors in Ψ. In this work, as in Ref. 56, $\Psi_{\perp}$ is written as a product of single-particle Gaussians, effectively treating the monolayer vibrational mode polarized in the surface-normal direction as a flat mode with no variation in frequency across the two-dimensional Brillouin zone.[42,56] This has been shown to be a good approximation.[42]

This Q2D approach involves an explicit assumption that the adatom finds the optimum z-position as it moves along the surface. This means that there is an implicit assumption being made about the coupling of the motion in z to that in $\boldsymbol{r}$. Given this, there are a number of avenues to the projection of the 3D potential energy of the BR model into the plane of $\boldsymbol{r}$, some purely classical in approach and some quantum in nature. The quantum projections build upon the classical projections by averaging various expressions of the classical projections over the zero-point (and thermal) motion of the adatom in the z-direction. That is, a quantum projection corresponding to any particular classical one replaces the potential energies (and their derivatives with respect to the z-displacement) with the appropriate quantum thermal averaging using the Self-Consistent Phonon (SCP) Gaussian distributions as specified in Refs. 56 and 57. This Q2D approach results in a modified form of the 3D Steele expansion of the potential energy of an atom due to the surface of a crystalline substrate,[9,58] using quantum thermal averaging to project the 3D potential energy into the plane of $\boldsymbol{r}$. This effective potential energy, denoted by $\tilde{U}(\boldsymbol{r})$, can be written as a Fourier series in the form

$$\tilde{U}(\boldsymbol{r}) = \sum_{\boldsymbol{G}} \tilde{U}_{\boldsymbol{G}} \exp(i\boldsymbol{G} \cdot \boldsymbol{r}), \quad (2)$$

where $\boldsymbol{G}$ is a reciprocal lattice vector of the two-dimensional surface lattice and the effective, Q2D Fourier coefficients $\tilde{U}_{\boldsymbol{G}}$ depend upon temperature as a result of the quantum thermal averaging of the xenon dynamics in the surface-normal direction (see the Appendix for the reciprocal lattice naming and indexing conventions used).

Our Q2D approach uses the quantum states that describe the $\Psi_{\perp}$ factor to calculate the Q2D Fourier coefficients that describe the variation of the substrate corrugation as a function of $\boldsymbol{r}$. The details of how this is done are described in the supplementary material which describes two quantum-based methods and three classical approximations.

There is an important caveat in this approach, and it is associated with the mixing of a classical treatment of the xy-motion with a quantum treatment of the z-motion. It is obvious how to deal with both the E_z and the E_{xy} terms since the first depends only on z (quantum treatment) and the second depends only on $\boldsymbol{r}$ (classical treatment). However, the E_{xyz} term depends upon both, so there is some ambiguity about how to properly treat this term because the effective Fourier coefficients defined by this term can reasonably be averaged over both the $\boldsymbol{r}$ and the z motions.[56] The decision was to match the MD and SCP energies (at zero temperature) as closely as possible by following the procedure in Ref. 56, even though this might overstate the effects of quantum and thermal smoothing at finite temperatures. On the other hand, this approach does come close to aligning the adatom-substrate classical potential energy with the corresponding SCP potential energy, even at finite temperatures. This approach can be interpreted as an approximate wave packet calculation. The approximations are 1. The replacement of the quantum thermal average of the Fourier term with a cumulant expansion as done in Ref. 59; 2. the use of constants for the second-order cumulants of the Gaussian distribution; and 3. using a separate SCP treatment of the $\sqrt{3}$ phase to determine these cumulants.[42] Additional details are to be found in the supplementary material.

B. Xenon-xenon interaction

The interaction between two isolated xenon atoms is taken to be the HFD-B2 interaction on p. 177 of Ref. 60, which

is a "Hartree-Fock-Dispersion" interaction.[7] This interaction does an excellent job of describing the various features of the xenon-xenon pair interaction in a vacuum. However, since the Xe atoms are adsorbed on a surface, there is a modification of this pair interaction generated by the dielectric properties of this surface. Thus, the HFD-B2 interaction is modified by adding a McLachlan interaction[31] with the parameters given by Bruch for the Pt(111) surface.[61] This model (HFD-B2+McLachlan) has been used successfully in Ref. 42 for a lattice dynamics analysis of this system and in Ref. 61 as part of the analysis of HAS experiments. In addition, as was the case in Ref. 42, the effects of any induced xenon dipole as well as three-body terms are ignored. Details, justification, and values of relevant parameters are given in Ref. 42 as is the justification for ignoring any dipole-dipole interactions. The parameter values in Ref. 42 are based on the work in Ref. 61.

C. Xenon-platinum interaction

The position of the preferred adsorption site, which is over the surface Pt atom, has an important effect on the stability of the various phases of Xe/Pt.[2,18,49,51,62–64] We choose the BR model to capture this aspect of the Xe/Pt system, as well as other important physical characteristics.[18] Furthermore, it is considered to be one of the more successful interaction models for this system, with much to recommend it.[1,2] It has been used in a successful treatment of the lattice vibrations for this system,[42,61,65] and the region of the potential well that is most important to lattice dynamics calculations has a similar importance here. The details of the implementation of this interaction model, including the parameters used for these calculations, are identical to those used in the lattice dynamics calculations of Ref. 42.

D. Molecular dynamics simulations

The simulations presented here are standard molecular dynamics simulations in 2D (fixed particle number, area, and total energy) with the substrate potential energy given by Eq. (2). The simulations are carried out using scaled equations with a length scale of 4.3656 Å, an energy scale of 282.8 K, and a time scale of 3.262 ps. The technical details of these simulations are found in the supplementary material. We have carried out a series of simulations for different sets of these Fourier coefficients, using a range of coefficients which should bracket the most likely values both at low temperatures and at high temperatures. It is our expectation that we have a bracket around the most likely behavior of the system for the range of temperatures of interest. Details and supporting arguments are found in Sec. III A and in the supplementary material.

We refer to the selections of different projections and system sizes as separate case studies, each being tagged using a notation that consists of two strings separated by a colon. The first string specifies the corrugation model for Xe/Pt and the second one specifies the size of the system. An example is the case study U25:65 K, where the U25 refers to a Fourier expansion with a single independent amplitude ($U_{(10)} = -25$ K) and the 65 K refers to the system having 65 536 particles in the box. A BR for the first string denotes the Barker-Rettner interaction as in cases 1 and 2 of Table I. Furthermore, if the first string is terminated by a "-H," as in BR-H, then that infers the case study is for an unconstrained geometry (hexagonal shaped patch). A "-U," as in BR-U, denotes an initial uniaxial configuration (striped phase) which was either unconstrained (i.e., rectangular patch for the 20 K size) or a constrained geometry (i.e., for the 65 K size). If there is no such designation, then the simulation is for a constrained geometry with the initial lattice being either hexagonal or centered-rectangular. The number density of the $\sqrt{3}$ structure, denoted by $\rho_0 = 0.050\,16$ Å^{-2}, is used to scale the density in various figures and tables.

TABLE I. Parameters that define typical case studies discussed in this work. All energy values are in kelvin.

Case study	Substrate	Projection	Size (K)	$U_{(10)}$
BR:65 K[a]	Pt(111)	BR	65	−35.6
BR-H:20 K[b]	Pt(111)	BR-H	20	−35.6
U25-H:20 K[b]	Pt(111)	U25-H	20	−25.0

[a]Constrained geometry with 65 536 adatoms.
[b]Unconstrained geometry with 20 064 adatoms.

III. RESULTS

The results of our simulations are organized as follows. In Sec. III A, we report and discuss the calculation of the parameters of the substrate corrugation. In Sec. III B, we define the different initialization phases that were studied, followed by an analysis of the ground state structure for constrained geometries in Sec. III B 1 and for unconstrained geometries in Sec. III B 2. In Sec. III B 3, we report calculations and analysis of the structure factor of the different case studies which is the figure of merit for the comparison to experimental results, reported in Sec. IV. Additional explanations, results, comparisons, and discussion are to be found in the supplementary material such as the details of the calculation of the corrugation that is the basis for the conclusions of Ref. 35.

A. Substrate corrugation

The descriptions and the corresponding Fourier coefficients used for the case studies examined here and in Ref. 35 are given in Tables I and II. The naming and indexing conventions used for the reciprocal lattices are described in the Appendix. The details of these calculations are to be found in the supplementary material. The origin (or zero) of the 2D energy calculation for a given case study is the corresponding value of E_z. These values are given in Table III for three temperatures, along with the minimum value of the laterally averaged substrate potential energy U_0 and the corresponding values of z_{opt}, the optimum value of z. As described in

TABLE II. The Fourier coefficients used in these MD calculations. All values are in kelvin.

Projection	$U_{(10)}$	$U_{(11)}$	$U_{(20)}$
BR[a]	−35.64	0.39	0.48
UN[b]	−*N*.00	...	...

[a]Calculated using the classical perturbation approach.
[b]N ∈ {20, 25, 30, 35}.

TABLE III. Parameters for the projection of the BR model onto the surface plane. The minimum in the laterally averaged potential well is U_0, the 1D total energy is E_z (includes SCP zero-point and thermal energies), and the corresponding optimum z-position for the laterally averaged substrate potential energy is z_{opt}. All energies are in units of 10^3 K and all distances are in Å.

Approach	U_0	E_z	z_{opt}[a]
Classical	−2.746	−2.746	3.43
Quantum[b]	−2.738	−2.730	3.44
Quantum[c]	−2.715	−2.684	3.48
Quantum[d]	−2.691	−2.636	3.52

[a]Optimized using only the U_0 term.
[b]$T = 0$.
[c]$T = 60$.
[d]$T = 110$ K.

Sec. II A, the quantum optimization uses SCP averaging, thus minimizing the free energy contribution associated with the z-motion.

For comparisons with experiment, we show the binding energy ϵ_0, the isosteric heat q_{st}, and the optimum z-position z_{opt} for the BR model as well as corresponding experimental values. These results are found in Table IV. The relations between q_{st} and the theoretical ϵ_0 are explained in the supplementary material.

The theoretical and experimental values of z_{opt} agree very well, while the corresponding values of q_{st} differ by about 5%–15%. The calculated values of the z-wise vibrational amplitude of the xenon motion for the $\sqrt{3}$ phase at 110 K are in excellent agreement with experiment, with theory giving 0.16 Å[42,66] and experiment giving 0.17 Å.[16] In all, the agreement between the BR model results and the experimental results is both respectable and satisfactory.

A comparison of the results for the calculation of the finite $\boldsymbol{G}$ Fourier coefficients, using the classical approach from Sec. II A and the supplementary material, is displayed in Table V. The first method produces a good estimate of $U_{(10)}$, quite compatible with that of the second method. The second method produces values of $U_{(11)}$ and $U_{(20)}$ that are rather small, but perhaps not completely negligible. The third method has a slightly different set of $U_{\boldsymbol{G}}$, but an overall corrugation that is not that different than the other two.

TABLE IV. Theoretical and experimental values for the binding energy ϵ_0, the isosteric heat of adsorption q_{st}, and the equilibrium separation of the isolated xenon atom from the platinum surface z_{opt}. The theoretical values are obtained by using up to three independent $U_{\boldsymbol{G}}$ coefficients with the SCP approximation for the z-wise single particle dynamics. All energies are in units of 10^3 K and all distances are in Å.

Source	ϵ_0	q_{st}	z_{opt}
Theory[a]	2.67	2.79	3.50
Theory[b]	2.70	2.90	3.41
Kern[c]	...	3.21–3.31	...
Diehl[d]	...	3.02–3.25	3.40

[a]This work: q_{st} for a 2D ideal gas using U_0 and $T = 80$ K.
[b]This work: q_{st} for a 2D lattice gas of 3D-Oscillators at $T = 70$ K.
[c]Reference 37: $T \geq 70$ K and coverage $\Theta \leq 0.03$.
[d]Reference 16: $T = 110$ K.

TABLE V. The Fourier coefficients calculated using the classical projections described in the supplementary material. All values are in kelvin.

Projection	$U_{(10)}$	$U_{(11)}$	$U_{(20)}$
Method 1	−34.16	...	...
Method 2	−33.37	−0.80	−0.54
Method 3	−35.64	0.39	0.48

Comparisons using the corresponding quantum projections are displayed in Table VI. At zero kelvin, there is a small reduction in the magnitude of the classical value of the Fourier coefficient for $\tilde{U}_{(10)}$ due to quantum effects. There are corresponding small changes in the (absolute) values of the others. At 110 K, the reduction in $U_{(10)}$ is significantly larger but still with small values for the others. Given these results, it would be reasonable to use a range of −35.0 K to −24.0 K as the appropriate one for $U_{(10)}$ values in the temperature range from zero to a bit over 110 K. However, this assumes that the adatom is able to maintain the optimal distance from the surface, even at the highest temperatures, and also assumes that there are no effects generated by the thermal excitation of the Pt surface itself (see the supplementary material). Without a direct calculation of these effects, we can only guess how important these might be. However, such a calculation would go far beyond the goals of this work. Instead, we have simply used an arbitrary lowering of the corrugation, using a $U_{(10)}$ of −20.0 K as a corrugation lower bound.[35] This approaches the smallest corrugation that is reasonable, based upon the results above and an observed $\sqrt{3}$ phase that is stable in the temperature range from 60 K through over 110 K. Lowering the corrugation too much destabilizes the $\sqrt{3}$ phase over much of that temperature range. Our lower bound preserves this stability, but it does represent a significant lowering of the corrugation. In a couple of special test cases, a $U_{(10)}$ of −15.0 K was also used, but nothing differed in any interesting way. These calculations and the values found in Tables V and VI were the ones used in Ref. 35.

Finally, calculations were carried out comparing theoretical and experimental root-mean-square (RMS) vibrational amplitudes of the xenon atoms in an attempt to better constrain the corrugation. However, the results were not useful in improving our estimate of this corrugation. These calculations and the corresponding results are described in the supplementary material. Some additional consequences of this smoothing

TABLE VI. The Fourier coefficients calculated using the quantum projections described in the supplementary material. The calculations were carried out for temperatures of 0, 60, and 110 K. All values are in kelvin.

Projection	$U_{(10)}$	$U_{(11)}$	$U_{(20)}$
Method 1[a]	−32.7	...	...
Method 2[a]	−31.9	−0.8	−0.6
Method 1[b]	−29.01	...	...
Method 2[b]	−27.49	−0.94	−0.87
Method 1[c]	−26.08	...	...
Method 2[c]	−23.85	−1.18	−0.83

[a]Calculated at 0 K.
[b]Calculated at 60 K.
[c]Calculated at 110 K.

of the corrugation with increasing temperature are to be found in Ref. 35. As shown in that paper, reductions in the corrugation are important to the understanding of the phase transitions in the Xe/Pt system.

B. Molecular dynamics

The implementation of the basic MD simulation is outlined in the supplementary material and closely follows Refs. 36 and 43. Using these simulations along with the free energy analysis as discussed in the supplementary material, we examine the stability, structure, and thermal behavior of the $\sqrt{3}$ phase, the striped incommensurate (SIC) phase, and the hexagonal incommensurate (HIC) initializations. Both aligned (AIC) and rotated (RIC) HIC structures are examined. In addition, the stability of structures having irregular and apparently pinned domain walls are examined and compared to the others. These "chaotic" structures will be referred to as "chaotic hexagonal" and "chaotic striped," even though it is not clear if they satisfy the strict definitions of a chaotic state. We examine these structures by initializing the system in these configurations and then following the simulations out to apparent thermal equilibrium. When possible, free energy comparisons are made between the various structures to determine the stable phase (this cannot be done for the constrained geometries). Some initializations into these structures produce stable (or meta-stable) disordered (chaotic) domain-wall structures. Comparisons of the details of this work to those of Refs. 36 and 43 are described in the supplementary material. In addition to the thermodynamic functions calculated in Ref. 36, calculations were carried out for the specific heat at constant area and the two order parameters: ψ_6 and ψ_0. The definitions and thermal behavior of these two order parameters are to be found in Refs. 35 and 36. Other details of the thermodynamic calculations as well as corresponding results are to be found in that same reference. Further details follow here and in the supplementary material.

1. Constrained geometry

Our MD simulations indicate that the ground state of the BR model is the $\sqrt{3}$ state. Furthermore, at finite misfits, the HIC phase is the stable phase. However, for small misfits, the SIC phase will strongly compete with the HIC phase and have nearly the same free energy (see the supplementary material for details). If the low temperature corrugation is smoother than about $U_{(10)} \approx -30$ K (the exact value dependent upon the importance of quantum effects), the IC phase becomes the stable low temperature phase and the ground state of the system. It is not unreasonable to speculate that, depending upon the actual smoothing due to quantum and thermal effects (and corrections to the BR model), it might be possible for this system to have a $\sqrt{3}$ ground state with significant competition from a SIC phase, a stable IC phase at higher temperatures (but less than about 60 K), and then a return to a stable $\sqrt{3}$ phase at roughly that temperature.

If the actual corrugation is well below the values above, but still stronger than about $U_{(10)} \approx -15$ K, the system would evolve from an IC low temperature phase to the $\sqrt{3}$ phase as the temperature increases. However, the temperature range of stability for the $\sqrt{3}$ phase is reduced as the corrugation decreases. For corrugations much lower than this $U_{(10)} \approx -15$ K lower limit, the system does not enter the $\sqrt{3}$ phase before the disordering temperature but rather remains in the IC phase until melting. Preliminary calculations of quantum corrections do not appear to alter this conclusion in any significant manner (the calculations indicating that the AIC and SIC states have nearly identical free energies at small misfits).[66]

2. Unconstrained geometry

Most simulations for the unconstrained geometry were carried out for a system size of 20 K. The thermodynamic behavior of the unconstrained geometry, in the (average) density range of 0.14–0.67 times ρ_0, is not very sensitive to variations in that density (provided the system is an isolated, single patch). Most of the data were taken with an average density of roughly 0.45–0.55 on this scale, but some simulations at the highest and lowest densities were used so that the sensitivity of the results to changes in the average density could be examined. Nothing of significance was found.

The thermodynamic stability analyses (see the supplementary material) of the various meta-stable structures in this system demonstrates that the $\sqrt{3}$ phase is the stable phase of both the BR-H and U30-H projections at low temperatures but that the SIC phase has nearly the same energy at low temperatures. Thus, while the $\sqrt{3}$ phase is the expected low temperature phase of the BR model for Xe/Pt, it will have strong competition from the SIC phase. This may be what drives the system into the observed "chaotic" domain structure that is observed in the simulations. Furthermore, even though simulations using the smaller corrugations in Table II show that the stable phase at very low temperatures would be an IC phase, the stable phase at higher temperatures, even for these smaller corrugations, is still the $\sqrt{3}$ phase. Using the corrugation values shown in Table II, the stable phase at temperatures just below the melting temperature does appear to be the $\sqrt{3}$ phase. The effects of quantum behavior and the implications for the determination of the stable state will be addressed in a future publication.[66] However, preliminary calculations indicate that the basic conclusions of the MD stability analysis shown here are not significantly altered by quantum effects as calculated by a SCP type analysis.[56,66] Finally, the transition from $\sqrt{3}$ ground state to IC ground state occurs at values of $U_{(10)}$ between −30 and −25 K, the actual value most likely closer to −25 than −30 K. However, this value is affected by quantum corrections and it needs a more careful examination. This will also be addressed in a future publication.[66]

3. Structure of the monolayer

The complexity of the monolayer structure makes its description somewhat difficult and cumbersome. Nevertheless, there are a number of characteristics of the monolayer that are useful to describe in detail, and this can be done with some confidence. Some of these details are to be found in the supplementary material and in the discussions below.

The structure factor for the $\sqrt{3}$ phase shows the expected behavior for both constrained and unconstrained geometries.

At low temperatures, the widths of the $S(\boldsymbol{Q})$ peaks are consistent with the size of the system and show the expected decrease in peak height and increase in peak width as the temperature is increased and the system becomes more disordered. Total loss of long-range order is obvious at the transition temperature to the disordered state.[35]

As for the striped phase, while it is possible to generate many stripes in the constrained geometry, it was not possible to generate more than six to eight stripes using the unconstrained geometry and a system size of 20 K. The structure factor peaks for this case, for both constrained and unconstrained geometries, possess strong satellites once there are more than a couple of domain walls in the system. The presentations of the experimental data for $S(\boldsymbol{Q})$ in Refs. 40 and 41 do not seem to show the existence of strong satellites as found in these MD simulations. It does appear that the existence of strong satellite peaks is inconsistent with the data since the experimental analysis assumed that the main (parent) peaks are the major contributors to the scattering intensity. The lack of strong satellite peaks is an indication that even if the experimental system is a SIC phase, it is not the one possessing many stripes. The main peaks for the simulated (MD) striped phase did show shifts from the $\sqrt{3}$ peak locations, although these shifts might not have a simple relation to the "misfit" and the main satellite peak was similar in intensity to the parent peak. While our comparisons of the MD results with the experimental data are more qualitative than quantitative, these comparisons did take into consideration peak locations, peak shapes, and peak intensities. We believe the conclusion that the experimental diffraction peaks are not consistent with the SIC phase of the BR model and are based on sound arguments.

As would be expected, peaks for the apparently chaotic phase show a variety of structures. Many of these are difficult to interpret but are reflective of the disorder in the system. Some peaks show similarities to the peaks shown in the HAS data[40] associated with the SIC phase, even though the MD system is not a striped structure. A good example of this is shown in Fig. 1, where the domain structure shown is an example of this chaotic phase. This figure shows the typical pattern of domains and domain walls for these states, where the definition of the three domain sublattices and the domain walls is to be found in Refs. 35 and 43. This chaotic structure was generated by initialization in a low temperature $\sqrt{3}$ patch configuration and then slightly rotating the patch (by about 2°) before starting the simulation. This system was first cooled and then heated. It is clear that this structure is not a striped phase, but the structure factor, as shown in Fig. 2, shows some similarity to the experimental $S(\boldsymbol{Q})$ as shown in Fig. 2 of Ref. 40. However, the $S(\boldsymbol{Q})$ peaks in the simulation results are sharper than those found in the experimental results and are also shifted in $\boldsymbol{Q}$-space.

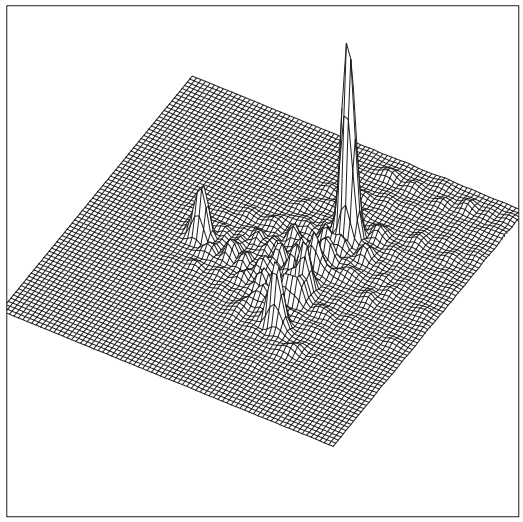

FIG. 2. 3D plot of $S(\boldsymbol{Q})$ for case study BR-H:20 K. The plot is for the region of $\boldsymbol{Q}$-space near the (02) peak of the $\sqrt{3}$ xenon monolayer. The origin is at the left corner, the x-axis is along the lower edge with $10.9 \le Q_x \le 11.9$, and the y-axis is along the left edge with $6.1 \le Q_y \le 7.1$. The initial rotation is 2° and the temperature is 2.922 K. The $\boldsymbol{Q}$ values are normalized by the length-scale as discussed in Sec. II D.

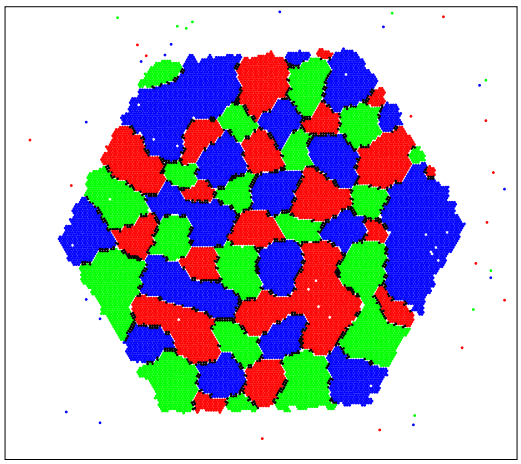

FIG. 1. Domain structure for case study BR-H:20 K. The initial rotation is 2° and the temperature is 2.922 K. Each shade (color) represents a domain of a different sublattice, while black (white) represents enhanced (reduced) density domain walls. See Ref. 43 for details.

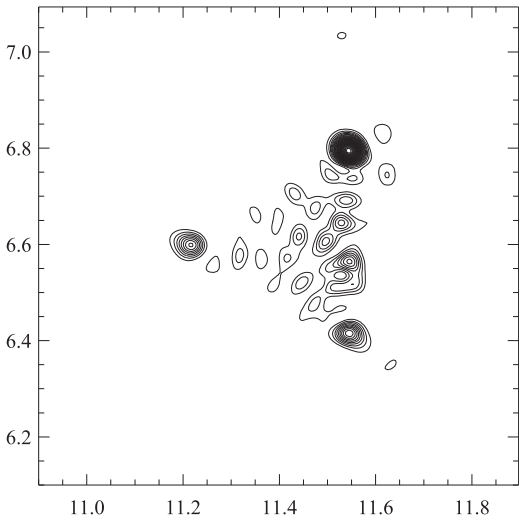

FIG. 3. Contour plot of $S(\boldsymbol{Q})$ for case study BR-U:20 K. The plot is for the region of $\boldsymbol{Q}$-space near the (02) peak of the $\sqrt{3}$ xenon monolayer. The horizontal axis is Q_x with $10.9 \le Q_x \le 11.9$, and the vertical axis is Q_y with $6.1 \le Q_y \le 7.1$. The initial rotation is 2° and the temperature is 2.922 K. The $\boldsymbol{Q}$ values are normalized by the length-scale as discussed in Sec. II D.

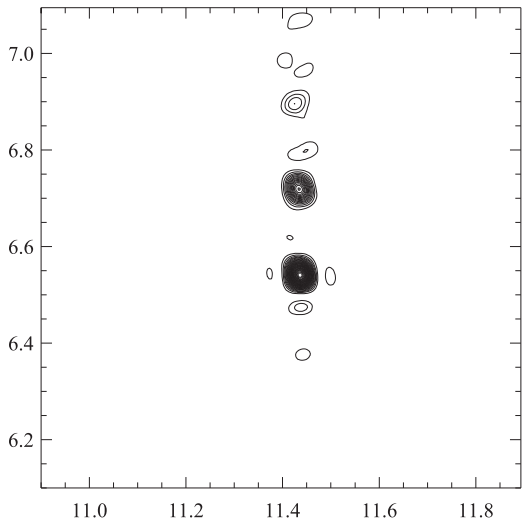

FIG. 4. $S(\boldsymbol{Q})$ for case study BR-U:20 K. The plot is for the region of $\boldsymbol{Q}$-space near the (02) peak of the $\sqrt{3}$ xenon monolayer. The horizontal axis is Q_x with $10.9 < Q_x < 11.9$, and the vertical axis is Q_y with $6.1 < Q_y < 7.1$. The initial configuration is striped and the temperature is 31.56 K. The $\boldsymbol{Q}$ values are normalized by the length-scale as discussed in Sec. II D. Note the high intensity of both the parent and main satellite peaks.

A contour plot of $S(\boldsymbol{Q})$ in the same region of $\boldsymbol{Q}$-space is shown in Fig. 3. The largest peak is about two or three times higher than the two smaller peaks, and the peak triplet is roughly centered near the xenon (02) peak of the $\sqrt{3}$ phase. This can be compared to the $S(\boldsymbol{Q})$ that results from a striped phase patch with five domain walls, as seen in Fig. 4. In the experiments, a triplet pattern was explained as an incoherent sum of contributions from three wall orientations rotated 120° from the others, with the peaks being generated from the shifted and unshifted parent peaks whose origins are the $\sqrt{3}$ peaks equivalent to the xenon (02) peak. Adding together three rotated contributions of the sort found in Fig. 4 would not give a triplet pattern.

IV. COMPARISON TO EXPERIMENT

Connections with the experimental results were investigated by calculations of the static structure factor $S(\boldsymbol{Q})$[36,43] for a selected subset of runs spaced along an appropriate range of temperatures. These calculations were compared to the experimental results to see if there are other possible interpretations of those experiments. Since the BR projection is the most appropriate one for the very low temperature range, the focus was on that projection using an unconstrained geometry with 20 K atoms in a single patch and having an average density of roughly $0.5\rho_0$. Results for the U35-H projection are essentially the same as the BR-H projection. We explored variations in the initialization of the system so as to generate a variety of initial structures. These variations used a series of initial rotations and initial densities (using the unconstrained geometry) to produce initial configurations of the SIC, AIC, and RIC structures. In addition, the response of the system to changes in the corrugation was investigated.

Simulations of the low temperature submonolayer solid show a system with extremely narrow domain walls that tend to zigzag in a rather haphazard and perhaps chaotic fashion.[34] The domain walls are often only two or three atoms in width, the width varying along the length of the wall. Some stretches of these walls exhibit wall widths which are effectively zero (that is, domains of different sublattices directly abut each other with a small gap). This is in marked contrast to the walls found in the Xe/Gr system, where the domain walls have a regular structure, are relatively wide, and are essentially of constant width.[36,43] Furthermore, the walls in the Xe/Pt system appear to be more erratic and not as easily categorized as domain wall models typically used in calculations found in the literature.[40,67,68] In addition, the walls seem to be rather resistant to movement (as evidenced by their propensity to stay near their original position as the system evolves). This happens both as the running time is increased and as the temperature is raised. Furthermore, this occurs even when a thermodynamic analysis clearly indicates that the state in question is not the one with the most thermodynamically stable structure. That is, these domain walls seem to stabilize meta-stable states, behaving as if they are pinned at low temperatures. As the temperature is raised above 60 K, these walls then appear to relax, causing the system to form a proper $\sqrt{3}$ structure with a couple of large domains (although often surrounded by some disorder as the temperature approaches the transition temperature).

The prediction of the BR model for the structure of the low temperature submonolayer is in stark contrast to both the HAS results and the STM results.[16,40,41,48] The existence of large patches of irregular but roughly hexagonal $\sqrt{3}$ domains separated by very narrow and irregular domain walls not only generates strong, single peaks at those scattering vectors $\boldsymbol{Q}$ that are coincident with the reciprocal lattice vectors $\boldsymbol{G}$ of the substrate but produces the triplet pattern shown in Fig. 2 for those $\boldsymbol{Q}$ not near such $\boldsymbol{G}$. However, the scattering pattern for the BR model, even with thermal smoothing, does look different from that shown in the experimental work of Kern.[40] Furthermore, these differences exist for both the "chaotic hexagonal" phase and the "chaotic striped" phase.

If one compares the $S(\boldsymbol{Q})$ for the "chaotic hexagonal" phase of the BR model to the experimental results, it is possible to see that the peaks in the vicinity of those $\boldsymbol{Q}$ vectors that are near corresponding reciprocal lattice vectors of the surface (for example, $\boldsymbol{Q} \approx \boldsymbol{\tau}_{(\bar{1}2)} \approx \boldsymbol{G}_{(01)}$) are actually not that different from the experimental results. The calculations show a strong, single peak at the location of the appropriate $\boldsymbol{G}$ vector (that is at the corresponding $\sqrt{3}$ phase $\boldsymbol{\tau}$ vector). The Kern data show a strong peak with (what is described as) a very weak and indistinct doublet. Here, the data are really not that different from the MD simulation. However, for the scattering peaks near the $\sqrt{3}$ phase $\boldsymbol{\tau}_{(02)}$ vector, the BR model shows a triplet centered about that location, while the Kern data show a triplet displaced significantly outward from this location. Furthermore, the peaks in the BR calculation are more distinct, possessing significantly smaller widths, than those found in the experimental results.[16,40,41,48]

Now, if one would instead examine the "chaotic striped" phase, looking at both the BR model and the Kern data, comparing $S(\boldsymbol{Q})$ for the "chaotic striped" phase to the experimental results, what is true of the "chaotic hexagonal" phase with regard to scattering near the $\boldsymbol{Q} \approx \boldsymbol{G}$ vectors is also true for the "chaotic striped" phase. Namely, the only significant intensity is at the corresponding $\sqrt{3}$ parent peak. However, for scattering near other peaks (like $\boldsymbol{\tau}_{(02)}$), the BR "chaotic striped" phase would show the pattern in Fig. 4 added (incoherently) with two others rotated by ±120°. This appears to be inconsistent with the Kern experimental results since, given the strong satellites shown in Fig. 4, the calculated peaks would not form a simple triplet pattern.

Since the predictions of the BR model, even with appropriate thermal smoothing, appear to be at odds with the experimental results, questions about just how the BR model could be deficient are relevant. In Ref. 35, a similar problem arose when comparing the experimental melting temperature and the prediction for the BR model. This same problem arose in the determination of the mobility of a xenon atom on the Pt(111) surface by quasi-elastic helium atom scattering (QHAS).[69] It does appear that there is a need for further smoothing of the corrugation beyond the thermal smoothing presented here. It can be suggested that this additional smoothing might be due to the thermal motion of the Pt(111) surface (see the supplementary material). But there also exists the possibility that the model corrugation is simply too strong and (or) the well width in the surface-normal direction is too narrow. Perhaps even at the very lowest temperatures, the basic BR model parameters need tweaking. With this in mind, we can examine the effects of lowering the corrugation along the same lines as done in Ref. 35.

For temperatures around 60 K, the BR value for $U_{(10)}$ is reduced (in magnitude) by thermal (and quantum) smoothing to about 28 or 29 K as can be seen in Table VI. This reduction is not sufficient to alter the scattering pattern in any significant way. However, if the value of $U_{(10)}$ were in the range from about −25 to −20 K, there is a significant shift in the position of the triplet surrounding the $\boldsymbol{\tau}_{(02)}$ peak. In particular,

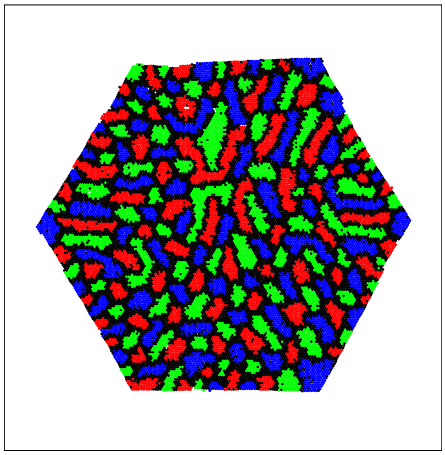

FIG. 5. Domain structure for case study U20-H:20 K. The initial rotation is 2° and the temperature is 45.26 K. Each shade (color) represents a domain of a different sublattice, while black (white) represents increased (reduced) density domain walls. See Ref. 43 for details.

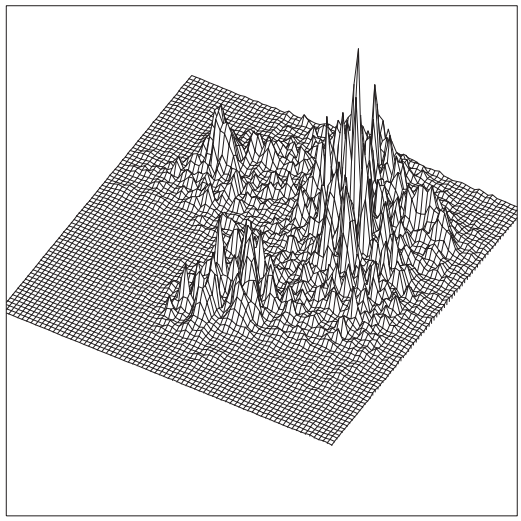

FIG. 6. 3D plot of $S(\boldsymbol{Q})$ for case study U20-H:20 K. The plot is for the region of $\boldsymbol{Q}$-space near the (02) peak of the $\sqrt{3}$ xenon monolayer. The origin is at the left corner, the x-axis is along the lower edge with $11.0 \le Q_x \le 13.0$, and the y-axis is along the left edge with $5.75 \le Q_y \le 7.75$. The initial rotation is 2° and the temperature is 26.4 K. The $\boldsymbol{Q}$ values are normalized by the length-scale as discussed in Sec. II D.

while there is still a triplet form to the pattern, the center of that pattern moves "outward" and beyond the $\sqrt{3}$ phase $\boldsymbol{\tau}_{(02)}$ position. The spatial domain pattern is similar to that shown in Fig. 1, but the domains are smaller and rather more irregular as can be seen directly in Fig. 5 (which is for the $U_{(10)} = -20$ K corrugation).

The $S(\boldsymbol{Q})$ for this state (at $T = 26.4$ K) is shown in Fig. 6. The peaks in $S(\boldsymbol{G})$ are lower and less distinct than in the BR case discussed above. Furthermore, the triplet is moved outward in $\boldsymbol{Q}$ space and shifted relative to the xenon $\sqrt{3}$ (02) peak instead of being centered on that peak location, as it is in the BR case. In fact, these peaks are quite similar to those in the experimental data.[40] It must be noted that there are many cases where the scattering pattern is different from those shown here, often being more disorganized and without sharp peaks as would be expected for a system with significant disorder. In particular, the state of the system appears to be sensitive to the history of state formation. This would be expected if the system is chaotic in nature, but the existence of this sensitivity in a MD simulation is not proof that the system is truly chaotic.

While structure factor calculations were not carried out for the "chaotic striped" phase with $|U_{(10)}| < 30$ K, an analysis using a different technique[36,59,70] suggests that $S(\boldsymbol{Q})$ for such states would still produce noticeable satellites. This would likely conflict with the patterns observed in the Kern experiments as discussed above. It should be noted that reducing the corrugation so that $U_{(10)} \approx -20$ K does not eliminate the meta-stability and "chaotic" behavior. However, doing so both increases the domain wall width and decreases the temperature range of stability for the $\sqrt{3}$ phase.

V. SUMMARY AND CONCLUSIONS

Our molecular dynamics simulations of submonolayer Xe on Pt(111), using the Barker-Rettner model combined with

the HFD-B2 Xe-Xe interaction as modified by the McLachlan interaction, show that the ground state of this model is the $\sqrt{3}$ structure. Furthermore, these BR model simulations clearly show that the equilibrium low temperature, low pressure phase is this same $\sqrt{3}$ phase. However, below approximately 60 K, this phase is susceptible to meta-stable chaotic disorder, creating domains of various irregular shapes and producing structure factors similar in nature to those of the HAS experiments.[40] The interpretation of the HAS scattering as confirming the existence of a striped phase as the low temperature structure may be a misinterpretation of the actual situation. Finally, these simulations show that this disorder anneals out as the temperature is raised above the 60 K mark, driving the chaotic system back into the $\sqrt{3}$ structure. It is from this higher temperature $\sqrt{3}$ phase that the system melts (disorders).[35]

The susceptibility to chaotic behavior is exhibited by a mix of disorganized hexagonal and striped domains in the same sample. The resulting $S(\boldsymbol{Q})$ near the xenon $\{10\}$ and $\{20\}$ peaks shows a triplet pattern that is similar in structure to that seen in HAS experiments.[32,40,41] On the other hand, for $S(\boldsymbol{Q})$ near the xenon $\{11\}$ peaks, the MD analysis shows essentially no difference between reflections from any of the examined phases (the $\sqrt{3}$, the HIC, the SIC, and the chaotic structures). All phases show a strong peak at the platinum 10 reflections, namely, just those found in the $\sqrt{3}$ phase. This is understandable since all these structures have the vast majority of the xenon atoms at or close to adsorption sites with, at most, only a few percent of these atoms in very narrow and irregular placed domain walls. Given that the $\sqrt{3}$ xenon $\{11\}$ peak set is coincident with the platinum $\{10\}$ peak set, all the xenon atoms at adsorption sites reflect in phase with each other at these values of $\boldsymbol{Q}$. These results contradict statements in Ref. 40 about the analysis of the scattering from the xenon $\{11\}$ peaks of the SIC structure, at least as it could be interpreted for the submonolayer case. Furthermore, the simulations of the model SIC phase show strong satellites in $S(\boldsymbol{Q})$, which contradicts that same experimental analysis for the $\{10\}$ and $\{20\}$ peaks.

There are, however, some problematic issues associated with the BR model, especially at higher temperatures. In particular, comparing simulation results to experimental results, there seems to be more smoothing of the corrugation with increasing temperature than can be accounted for within this model. The effect of this reduced corrugation on the thermodynamic behavior is examined in detail in Ref. 35, but this behavior is also found in quasi-elastic helium atom scattering (QHAS) experiments which can examine the diffusion of a Xe adatom on the Pt(111) surface.[69] The quasi-two-dimensional approach we used, combining a classical treatment of the monolayer dynamics parallel to the surface with a quantum treatment of the dynamics perpendicular to the surface, does help mitigate these problems, but it does not fully resolve all the issues. Our investigation of the thermodynamic and structural properties, comparing our calculations to previous simulations and known experimental results of this system and other systems, indicates that there is more thermal smoothing near the melting temperature than can be accounted for by current models. This is in stark contrast to other systems, such as Xe/Gr, where the same approach does an excellent job of explaining the experimental results.[36]

Further experimental studies are important for progress in the understanding of this system. In particular, work that can better examine the very low temperature corrugation of this system and probe the Xe/Pt potential energy surface is needed. For example, a careful experimental study of single-particle diffusion from very low temperatures up through melting, combined with corresponding simulations which include quantum corrections at low temperatures, could go a long way to the determination of the corrugation and its dependence on temperature. Improved *ab initio* studies of the xenon-platinum potential energy surface would be very useful, although the precision needed may be beyond the limits of current theoretical analysis.[19] Calculations of the effects of the thermal motion of the Pt(111) surface on the behavior of the xenon monolayer could be critical to the understanding of this problem. It is also important to do an experimental study of the effects of surface dynamics on the surface corrugation as the temperature is raised. It is possible that the dynamics of the platinum surface significantly influences the dynamics of the xenon monolayer at high temperatures by significantly smoothing the surface corrugation. Also important is the study of similar systems, namely, heavy noble gases adsorbed on strongly corrugated substrates having dilated adsorbate lattices. One such example could be submonolayer xenon adsorbed on Ru(001).[71] Furthermore, the structural analysis of the scattering from these systems must include an examination of possible chaotic states of the sort observed in these simulations.

The BR model does a good job of explaining the low temperature behavior of the xenon monolayer on the Pt(111) surface. However, while it is able to reproduce a significant collection of data, it is clear that getting the transition temperature for melting right and explaining the scattering data, the STM data, and the QHAS data requires alterations in or enhancements to the BR model at high temperatures. While reducing the corrugation does effect the phonon spectrum,[42] a simple SCP calculation shows that reducing the corrugation from the BR value to $U_{(10)} \approx -20$ K reduces the in-plane zone-center phonon gap by about 25% and produces a small increase in the maximum in-plane phonon energy.[66] However, these shifts look to be borderline tolerable as to the maintaining of the agreement with the previously calculated phonon energies and the experimental data.[42,61] For all its many successes, the BR model seems to need improvements of the sort discussed here.

SUPPLEMENTARY MATERIAL

See supplementary material for additional justifications, explanations, calculations, figures, and tables. This material includes discussions of (1) additional background information about this system; (2) details of the simulation methodology; (3) details of the free energy analysis; (4) details on the calculations of the Q2D Fourier coefficients; (5) calculations of the binding energies and heats of adsorption; (6) RMS vibrational analysis of the xenon monolayer; (7) estimates of the effects of the platinum surface dynamics; (8) additional results and discussions of the simulations.

TABLE VII. Equivalence mapping of the reciprocal lattice indexing used in other sources.

Lattice type	Kern[a]	Maps into	This work
Platinum	$(\bar{1}\bar{1})$	$\Longleftrightarrow$	(10)
Xenon	$(\bar{1}\bar{2})$	$\Longleftrightarrow$	(11)
Xenon	$(\bar{1}\bar{1})$	$\Longleftrightarrow$	(10)
Xenon	$(\bar{2}\bar{2})$	$\Longleftrightarrow$	(20)

[a]As described in Ref. 39.

ACKNOWLEDGMENTS

We would like to thank L. W. Bruch for probing discussions, insightful questions, and useful suggestions. We would like to acknowledge and thank C. Chen and S. Kapita for the work they did on the preliminary studies that preceded and motivated this work. We thank Lafayette College for its generous support and the Computer Science Department of Lafayette College for use of their research computer cluster. J.B.'s exchange visit to Lafayette College during the 2012 calendar year was sponsored by the Brazilian government agency Coordenação de Aperfeiçoamento de Pessoal de Nível Superior (CAPES) as part of the Science Without Borders program. J.B. acknowledges funding from the Austrian Science Fund (FWF) through the START Project No. Y879-N27.

APPENDIX: DIFFRACTION PEAK INDEX MAPPINGS

We are using the convention that the primitive translation vectors for both the xenon lattice and the Pt(111) lattice are placed 120° apart. Thus, the primitive reciprocal lattice vectors for both lattices ($\boldsymbol{\tau}$ for the xenon and $\boldsymbol{G}$ vectors for the platinum) are 60° apart. As a result, the magnitude of $\boldsymbol{G}_{(11)} = \boldsymbol{G}_{(10)} + \boldsymbol{G}_{(01)}$ is $\sqrt{3}$ times the magnitude of $\boldsymbol{G}_{(10)}$, and the same is true for the $\boldsymbol{\tau}$ vectors. This is in contrast with some of the referenced experimental work, where the opposite convention is used. Furthermore, there is a 30° rotation and sometimes an inversion between the reciprocal lattices used here and some of the experimental references. In addition, the SIC experimental data are an incoherent sum of peaks from three different orientations of the SIC walls, while the $S(\boldsymbol{Q})$ peaks presented here are those of a system with a single orientation. Therefore, some care must be exercised when comparing the simulation results to the experimental ones. In particular, the convention used here for the reciprocal lattice vector indexing differs from that used in the experimental work of Kern and co-workers.[39] This work uses an angle of 60° between the primitive reciprocal lattice vectors and the experimental work uses an angle of 120°. Table VII shows the mapping between the indices used in this work and that used in Ref. 39.

[1]L. W. Bruch, M. W. Cole, and E. Zaremba, *Physical Adsorption, International Series of Monographs on Chemistry* (Oxford University Press, New York, 1997), No. 33.
[2]L. W. Bruch, R. D. Diehl, and J. A. Venables, Rev. Mod. Phys. **79**, 1381 (2007).
[3]P. Corboz, M. Boninsegni, L. Pollet, and M. Troyer, Phys. Rev. B **78**, 245414 (2008).
[4]J. Ahn, H. Lee, and Y. Kwon, Phys. Rev. B **93**, 064511 (2016).
[5]M. Morishita, J. Low Temp. Phys. **187**, 453 (2017).
[6]L. Madeira and S. A. Vitiello, Surf. Sci. **655**, 39 (2017).
[7]R. A. Aziz, in *Inert Gases: Potentials, Dynamics, and Energy Transfer in Doped Crystals*, Vol. 34 of Springer Series in Chemical Physics, edited by M. L. Klein (Springer, New York, 2011), p. 5.
[8]L. W. Bruch, Surf. Sci. **125**, 194 (1983).
[9]W. A. Steele, "The interaction of gases with solid surfaces," in *Topic 14: Properties of Interfaces. The International Encyclopedia of Physical Chemistry and Chemical Physics* (Pergamon Press, Oxford, New York, 1974), Vol. 3.
[10]G. Vidali, G. Ihm, H.-Y. Kim, and M. W. Cole, Surf. Sci. Rep. **12**, 135 (1991).
[11]A. P. Jardine, S. Dworski, P. Fouquet, G. Alexandrowicz, D. J. Riley, G. Y. H. Lee, J. Ellis, and W. Allison, Science **304**, 1790 (2004).
[12]W. W. Hayes and J. R. Manson, Phys. Rev. Lett. **109**, 063203 (2012).
[13]D. Farias and K.-H. Rieder, Rep. Prog. Phys. **61**, 1575 (1998).
[14]A. J. Gellman, L. Baker, and B. S. Holsclaw, Surf. Sci. **646**, 83 (2016).
[15]D.-L. Chen, W. A. Al-Saidi, and J. K. Johnson, J. Phys.: Condens. Matter **24**, 424211 (2012).
[16]R. D. Diehl, T. Seyller, M. Caragiu, G. S. Leatherman, N. Ferralis, K. Pussi, P. Kaukasoina, and M. Lindroos, J. Phys.: Condens. Matter **16**, S2839 (2004).
[17]T. Seyller, M. Caragiu, R. D. Diehl, P. Kaukasoina, and M. Lindroos, Phys. Rev. B **60**, 11084 (1999).
[18]J. A. Barker and C. T. Rettner, J. Chem. Phys. **97**, 5844 (1992); **101**, 9202 (1994).
[19]A. Betancourt and D. Bird, J. Phys.: Condens. Matter **12**, 7077 (2000).
[20]K. S. Liang, K. L. D'Amico, C. H. Lee, and E. Y. Sheu, Phys. Rev. Lett. **65**, 3025 (1990).
[21]M. H. Jensen and P. Bak, Phys. Rev. B **27**, 6853 (1983).
[22]P. Bak, Rep. Prog. Phys. **45**, 587 (1982).
[23]R. Hobart, J. Appl. Phys. **36**, 1948 (1965).
[24]R. Hobart, J. Appl. Phys. **36**, 1944 (1965).
[25]J. M. Ziman, *Electrons and Phonons*, The Theory of Transport Phenomena in Solids (University Press, Oxford, 1972).
[26]B. Joos, Solid State Commun. **42**, 709 (1982).
[27]R. D. Boutchko and L. W. Bruch, Phys. Rev. B **70**, 195422 (2004).
[28]N. Varini, A. Vanossi, R. Guerra, D. Mandelli, R. Capozza, and E. Tosatti, Nanoscale **7**, 2093 (2015).
[29]D. Mandelli, A. Vanossi, N. Manini, and E. Tosatti, Phys. Rev. B **95**, 245403 (2017).
[30]R. Guerra, M. van Wijk, A. Vanossi, A. Fasolino, and E. Tosatti, Nanoscale **9**, 8799 (2017).
[31]A. D. McLachlan, Mol. Phys. **7**, 381 (1964).
[32]K. Kern, R. David, R. L. Palmer, and G. Comsa, Appl. Phys. A **41**, 91 (1986).
[33]K. Kern, in *Phase Transitions and Adsorbate Restructuring at Metal Surfaces*, Vol. 7 of The Chemical Physics of Solid Surfaces, edited by D. A. King and D. P. Woodruff (Elsevier Science, New York, 1994), p. 299.
[34]A. D. Novaco, C. Chen, and S. Kapita, "Chaotic pinning of a xenon monolayer on a Pt(111) surface" (unpublished).
[35]A. D. Novaco, L. W. Bruch, and J. Bavaresco, Phys. Rev. B **91**, 161412 (2015).
[36]A. D. Novaco and L. W. Bruch, Phys. Rev. B **89**, 125431 (2014).
[37]K. Kern, R. David, P. Zeppenfeld, and G. Comsa, Surf. Sci. **195**, 353 (1988).
[38]G. Comsa, K. Kern, and B. Poelsema, in *Helium Atom Scattering from Surfaces*, Vol. 27 of Springer Series in Surface Sciences, edited by E. Hulpke (Springer-Verlag, New York, 1992), p. 24.
[39]K. Kern, R. David, R. L. Palmer, and G. Comsa, Phys. Rev. Lett. **56**, 620 (1986).
[40]K. Kern, R. David, P. Zeppenfeld, R. Palmer, and G. Comsa, Solid State Commun. **62**, 391 (1987).
[41]K. Kern, Phys. Rev. B **35**, 8265 (1987).
[42]L. W. Bruch and A. D. Novaco, Phys. Rev. B **61**, 5786 (2000).
[43]L. W. Bruch and A. D. Novaco, Phys. Rev. B **77**, 125435 (2008).
[44]J. E. Black and P. Bopp, Surf. Sci. **182**, 98 (1987).
[45]J. E. Black and P. Bopp, Phys. Rev. B **34**, 7410 (1986).
[46]J. E. Black and A. Janzen, Langmuir **5**, 558 (1989).
[47]J. E. Black and A. Janzen, Phys. Rev. B **39**, 6238 (1989).
[48]F. Brunet, R. Schaub, S. Fedrigo, R. Monot, J. Buttet, and W. Harbich, Surf. Sci. **512**, 201 (2002).
[49]J. M. Gottlieb, Phys. Rev. B **42**, 5377 (1990).
[50]J. M. Gottlieb and L. W. Bruch, Phys. Rev. B **44**, 5759 (1991).
[51]J. M. Gottlieb and L. W. Bruch, Phys. Rev. B **44**, 5750 (1991).
[52]E. Flenner and R. D. Etters, Phys. Rev. Lett. **88**, 106101 (2002).

[53]E. Flenner and R. D. Etters, Phys. Rev. B **73**, 125419 (2006).
[54]E. A. Ustinov and D. D. Do, Adsorption **20**, 439 (2014).
[55]E. A. Ustinov, J. Chem. Phys. **140**, 074706 (2014).
[56]A. D. Novaco, Phys. Rev. B **46**, 8178 (1992).
[57]A. D. Novaco, Phys. Rev. Lett. **60**, 2058 (1988).
[58]W. A. Steele, Surf. Sci. **36**, 317 (1973).
[59]A. D. Novaco, Phys. Rev. B **19**, 6493 (1979).
[60]A. K. Dham, W. J. Meath, A. R. Allnatt, R. A. Aziz, and M. J. Slaman, Chem. Phys. **142**, 173 (1990).
[61]L. W. Bruch, A. P. Graham, and J. P. Toennies, J. Chem. Phys. **112**, 3314 (2000).
[62]P. Rejto and H. C. Andersen, J. Chem. Phys. **98**, 7636 (1993).
[63]J. F. Weaver, J. A. Stinnett, and R. J. Madix, Surf. Sci. **391**, 150 (1997).
[64]T. Seyller, M. Caragiu, R. D. Diehl, P. Kaukasoina, and M. Lindroos, Chem. Phys. Lett. **291**, 567 (1998).
[65]L. W. Bruch, A. P. Graham, and J. P. Toennies, Mol. Phys. **95**, 579 (1998).
[66]A. D. Novaco, "Direct-space self-consistent phonon analysis of monolayer structures and dynamics" (unpublished).
[67]E. D. Specht, A. Mak, C. Peters, M. Sutton, R. J. Birgeneau, K. L. D'Amico, D. E. Moncton, S. E. Nagler, and P. M. Horn, Z. Phys. B **69**, 347 (1987).
[68]M. Kardar and A. N. Berker, Phys. Rev. Lett. **48**, 1552 (1982).
[69]J. Ellis, A. P. Graham, and J. P. Toennies, Phys. Rev. Lett. **82**, 5072 (1999).
[70]A. D. Novaco, Phys. Rev. B **22**, 1645 (1980).
[71]B. Narloch and D. Menzel, Surf. Sci. **412-413**, 562 (1998).

Supplement to: "Simulations of submonolayer Xe on Pt(111): the case for a chaotic low temperature phase"

Anthony D. Novaco[1, a)] and Jessica Bavaresco[2, b)]
[1)] *Department of Physics, Lafayette College*
Easton, Pennsylvania 18042, USA
[2)] *Institute for Quantum Optics and Quantum Information (IQOQI)*
Austrian Academy of Sciences, Boltzmanngasse 3, A-1090 Vienna, Austria

(Dated: 21 January 2018)

This supplement contains additional justifications, explanations, calculations, figures, and tables to accompany the above paper by Novaco and Bavaresco.

PACS numbers: 68.43.-h, 68.35.Md, 68.35.Rh, 64.70.Rh
Keywords: adsorption, monolayers, xenon, Pt(111), graphite, molecular dynamics, chaos

I. INTRODUCTION

We investigate whether chaotic behavior at low-temperatures can be present in a case of physical adsorption; proposing that such is the case for Xe/Pt, contrary to the common wisdom for this system.[1] This xenon monolayer exhibits very narrow domain walls with little distortion in the ideal placement of the xenon atoms in the two domains on either side of the wall; such behavior being driven by the strong corrugation and the dilated adlayer lattice structure of this system. It is this characteristic that most likely generates the criteria needed to drive chaotic behavior in this system. The domain wall behavior in this system is consistent with these walls being pinned, at low temperature, by the Peierls force; this pinning force then being significantly reduced as the temperature of the system is increased, causing the system to become more ordered.

The points just raised imply that a re-examination of this system is appropriate. Given what we now know of the mutual interaction between Xe gas atoms, the modification of this interaction by the substrate surface, and the interaction between these atoms and the Pt(111) surface, this re-examination is both justified and timely. Furthermore, today's computational capabilities allow the simulation of much larger systems then what was possible in the past. In the case of Xe/Pt, this is important because some of the more interesting effects shown here and elsewhere[2] would not appear in the small systems examined in the older works.

This supplement contains detailed discussions of the methodology of the simulations, the explanation of the free energy analysis, details of the calculations for the Q2D Fourier coefficients, calculations and results for the RMS vibrational amplitudes of the xenon adatom, discussion of the effects of platinum surface dynamics on the dynamics of the xenon submonolayer, additional details of the results, and additional discussions of these results.

II. SIMULATION METHODOLOGY

The basics of the MD simulation are the same as those in Refs. [3 and 4], using essentially the same code with mostly the same set of parameters. As in those works, we examine both the constrained geometry (a single phase filling the simulation box) and the unconstrained geometry (an isolated patch surrounded by vapor). Constrained-geometry simulations are used to determine the stable low temperature phase for the classical system, and to examine the system in a simple context (the constrained geometry having only one phase present at any given temperature).[2] These simulations of the constrained geometry are also useful in the interpretation of the high temperature behavior of the unconstrained-geometry simulations.[2] Simulations of the unconstrained-geometry are carried out to examine both the thermal behavior and the structural properties of the submonolayer patch. The system sizes chosen were different from Ref. [3], with the largest system reported here being a constrained geometry with 65536 adatoms (65K). Most of the simulations of the unconstrained geometry contained 20064 adatoms (20K). Smaller systems having 4096 and 16384 adatoms (4K and 16K) were also used to check for size dependencies.

The simulations were carried out using scaled equations with a length scale of 4.3656 Å, an energy scale of 282.8 K, and a time scale of 3.262 ps. The scaling, time step, force truncation details, nearest-neighbor shells, criteria for determining equilibrium, and the criteria for averaging are the same as the earlier works cited. The main difference in the behavior of these MD simulations compared to those referenced above, is the existence of significant meta-stability in these results that did not appear to occur in the previous work (except for the largest corrugation reported in that work). Relaxation times for the Xe/Pt simulations are much longer than those found for Xe/Gr, which we attribute to the stronger corruga-

[a)] E-mail: novacoad@lafayette.edu
[b)] E-mail: jessica.bavaresco@oeaw.ac.at

tion in the Xe/Pt system. The average densities for the unconstrained geometry varied over a wider range in this study then in Ref. [3]. Here the lower bound is $0.14\rho_0$ and the upper bound is $0.67\rho_0$, with the typical simulation carried out at $\approx 0.50\rho_0$.

The data was collected in blocks of 1000 time steps (32.6 ps), each time step being 0.01 scaled time units. In most cases, blocks 400–500 (13.04–16.30 ns) were used to calculate the thermodynamic functions as before. Some selective runs were carried out to nearly 1500 blocks (48.90 ns). Structure factor calculations typically used blocks 500–600 (16.30–19.56 ns), selecting about 25 to 50 configurations, uniformly spaced in time, from that set of blocks. The determination of the stable state is obtained by initializations of the system in various structures and running until the run has stabilized. Equilibrium data was typically taken only after this stabilization. A given simulation was typically run for at least 13.0 ns before being either heated or cooled to the next energy. Each run was then continued until equilibrium was attained. The usual tests were performed to determine if a given run has stabilized.[5]

The starting point for the $\sqrt{3}$, AIC, and RIC unconstrained configurations is a hexagonal patch centered in the simulation box. The initial patch density was adjusted by altering the lattice parameter of the patch, and RIC configurations were generated by initial rotations of the patch away from the $\sqrt{3}$ orientation. The SIC initializations (for the unconstrained systems) were rectangular patches with the $\sqrt{3}$ orientation, commensurate with the platinum structure in the xenon $[1, 0]$ direction but compressed in the perpendicular direction. The striped structures so generated typically had 2 to 8 domain walls. Attempts to initiate unconstrained striped configurations with more than 8 walls result in systems that are mechanically unstable and collapse into structures that are very disordered and have higher free energy at a given temperature than the $\sqrt{3}$ structure. Attempts to initialize an unconstrained case with too high a patch density also produces unstable runs that abort with a corresponding of loss of energy conservation. The sensitivity of the results to system size was tested by doing simulations of the constrained geometry for 4K, 16K, and 65K sizes. There is little observable difference in the thermodynamics generated for those cases when far from the melting transition, although this is not strictly true, as explained in the Sec. VIII A, for ψ_0 near the melting transition.

We did not study the approach to equilibrium near the melting transition carefully, but we did carry out extensive testing of the sensitivity of these results to the initialization of the system. These initializations involved changing the density, the orientation of the adatom layer relative to the surface (the rotation angle), and the geometry of the domain walls so generated (striped vs hexagonal). The relevant results are described in Ref. [2], in the main article, and here in Sec. VIII.

To test the convergence of the $S(\boldsymbol{Q})$ results, calculations were performed using the $\sqrt{3}$ structure, a 20K system, and configurations from blocks 600 to 1100. These calculations show that, in general, it is only necessary to use from 25 to 50 configurations, uniformly spaced over about 100 blocks, to obtain good statistics. A larger sample set is not necessary for a reliable $S(\boldsymbol{Q})$ calculation. Peaks for the (10), (01), $(\bar{1}1)$, $(\bar{2}1)$, $(\bar{1}2)$, (02), and some others equivalent to these were generated and examined. Calculations were also carried out for selected $\sqrt{3}$ and striped structures of the constrained geometry. The results were as expected.

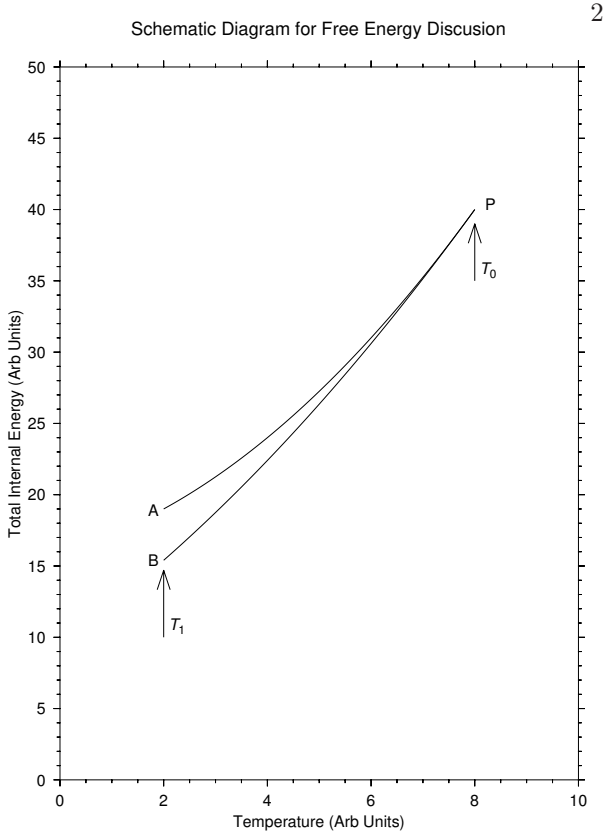

FIG. 1. Points A and B, both at a temperature T_1, are terminal points for the corresponding paths. Point P, the common endpoint for both paths, is at a temperature T_0. Both paths describe constant area processes along lines of presumed stable or meta-stable states.

III. FREE ENERGY ANALYSIS

Consider two paths in the energy-temperature plane, as shown in Fig. 1, that have a common point P having a temperature of T_0. The combined path (A plus B) describes a constant area process which both starts and ends at points which have a temperature of T_1. Let path A be above path B, that is path A has the higher energy at each temperature. Now assume that each path represents a distinctly different structure for the system, with each path being associated with a distinctly different region of phase space. However, at the common point P, assume that the two paths describe a common region of phase space, thus a common phase of the sys-

tem. Assume that each path represents a meta-stable system that, in the spirit of a restricted ensemble analysis, can be described by equilibrium thermodynamics. Also, allow for the possibility that one branch is actually the stable equilibrium state of the system. The question is: which of the two paths represents the stable (or more stable) branch?

Consider a path which traverses path B from T_1 to T_0, then moves along path A from T_0 to T_1. Start with the identity

$$f_A - f_B = (\epsilon_A - \epsilon_B) - T_1\,(s_A - s_B)$$

where f, ϵ, and s are the Helmholtz free energy, the internal energy, and the entropy (each per particle). We assign points B and A to represent the corresponding endpoints of the path first along path B through P and then along path A, Now, if c_a is the specific heat (per particle) at constant area, then along either path we have

$$\epsilon_f - \epsilon_i = \int_{T_i}^{T_f} \mathrm{d}T\; c_a \quad \text{and} \quad s_f - s_i = \int_{T_i}^{T_f} \mathrm{d}T\; \frac{c_a}{T}.$$

Using the relations above, we generate a simple relation between the free energy at point A and that of point B, namely:

$$f_A - f_B = \int_{T_1}^{T_0} \mathrm{d}T\; \left[1.0 - \frac{T_1}{T}\right] \left[c_a^B - c_a^A\right], \qquad (1)$$

where the superscript on c_a refers to the path taken. The case shown in Fig. 1 illustrates the case most often found in these simulations. In particular, the path with the higher energy also has the smaller specific heat (smaller slope) with the paths merging at some higher temperature. Thus in Eq. (1), we have $T_1 \le T$ and $c_a^B > c_a^A$, which implies that $f_A > f_B$ and the lower path is not only the one of lower energy, it is also the one with the lower free energy. Conclusion: the lower path is the more stable one when $T_1 < T_0$.

For the $T_1 > T_0$, imagine the paths in Fig. 1 inverted about point P, with path B possessing the higher energy, but still possessing the larger c_a. Repeating the analysis for this case, the end result is similar to Eq. (1), but has a sign change. The result is:

$$f_A - f_B = \int_{T_0}^{T_1} \mathrm{d}T\; \left[\frac{T_1}{T} - 1.0\right] \left[c_a^B - c_a^A\right]. \qquad (2)$$

With $T_1 > T_0$ and $c_a^B > c_a^A$: $f_A > f_B$. Therefore, path B is still the stable path. That is, for $T_1 > T_0$, the upper path is now the stable one. These arguments are similar to those found in Ref. [6], starting on page 296.

IV. Q2D FOURIER COEFFICIENTS

The Q2D approach starts with the Steele expansion of the potential energy of an atom due to the surface of a crystalline substrate.[7,8] This potential energy, denoted by $U(\boldsymbol{r}, z)$, can be written as a Fourier series of the form:

$$U(\boldsymbol{r}, z) = \sum_{\boldsymbol{G}} U_{\boldsymbol{G}}(z) \exp(i\boldsymbol{G}\cdot\boldsymbol{r}), \qquad (3)$$

where $\boldsymbol{G}$ is a reciprocal lattice vector of the two-dimensional surface lattice (See Appendix A in the main article for the naming and indexing conventions used). It should be noted that the model presented here does not depend upon the $U_{\boldsymbol{G}}(z)$ having any particular form, only that each be expressed in some manner that allows the calculation of the corresponding derivatives with respect to the z-coordinate. Therefore, it is possible to use this approach in conjunction with any potential energy model for the adatom-substrate interaction and not just for the site-site model that is used in this communication.

The Fourier components that define the corrugation of the surface are dependent on z, so if the adatom were to move along the surface following the path of minimum energy, it would move perpendicular to the surface as it moves parallel to the surface. If this is treated as a purely classical problem, there are a couple of ways to proceed. The simplest method, and the one often used,[9] is to find the minimum barrier to translation moving from one adsorption site to the next and ascribe this to the simplest form of Eq. (3):

$$U(\boldsymbol{r}) = U_{(10)} \sum_{\boldsymbol{G}} \exp(i\boldsymbol{G}\cdot\boldsymbol{r}), \qquad (4)$$

where $U_{(10)}$ is a constant, and the sum over $\boldsymbol{G}$ is now only over the six reciprocal lattice vectors equivalent to $\boldsymbol{G}_{(10)}$. A somewhat improved (but more complicated) approach, is to first calculate (for hexagonal lattices) four specific values from Eq. (3); these being the minimum value of $U_0(z)$ and the minimum potential energies over the Atop site, the hollow site, and the bridge site. These energies are denoted by U_0, U_A, U_H and U_B respectively with the corresponding z-value denoted by a corresponding z_{opt}. From these four energies, the three independent Fourier coefficients $U_{(10)}$, $U_{(11)}$, and $U_{(20)}$ can be obtained if it is assumed that the higher-order coefficients can be ignored. For the simple hexagonal lattice (i.e. Pt(111), we find:

$$U_{(10)} = 5\delta U_A/72 - \delta U_B/8 - \delta U_H/9 \qquad (5a)$$

$$U_{(11)} = (\delta U_A + 2\delta U_H)/18 \qquad (5b)$$

$$U_{(20)} = (\delta U_A + 3\delta U_B)/24 \qquad (5c)$$

where $\delta U_A \equiv U_A - U_0$, $\delta U_B \equiv U_B - U_0$, and $\delta U_H \equiv U_H - U_0$. Similar equations hold for the open-hexagonal-net lattice (i.e. graphite) with the exchange of δU_A with δU_H. For Xe/Pt, direct calculations show that the second and third coefficients are much smaller than the first.

A third approach is a perturbation calculation for the displacements of the xenon atoms in the z-direction, using a Fourier series expansion for the optimum z-position and a Taylor series expansion of the $U_{\boldsymbol{G}}(z)$ to second order. It is then possible to define effective 2D Fourier

coefficients $\tilde{U}_{\boldsymbol{G}}$ and easily show that:

$$\sum_{\boldsymbol{G}_1} U^{zz}_{\boldsymbol{G}-\boldsymbol{G}_1}(z_0) Z_{\boldsymbol{G}_1} = -U^{z}_{\boldsymbol{G}}(z_0) \tag{6a}$$

and

$$\tilde{U}_{\boldsymbol{G}} \equiv U_{\boldsymbol{G}}(z_0) + \frac{1}{2}\sum_{\boldsymbol{G}_1} U^{z}_{\boldsymbol{G}-\boldsymbol{G}_1}(z_0) Z_{\boldsymbol{G}_1} \tag{6b}$$

where the $Z_{\boldsymbol{G}}$ are the Fourier amplitudes of the displacements in the z-direction relative to z_0 and the $U^{z}_{\boldsymbol{G}}$ and $U^{zz}_{\boldsymbol{G}}$ are the first and second derivatives of the $U_{\boldsymbol{G}}(z)$. The expansion point z_0 is the z-position of the minimum in $U_0(z)$.

The quantum projections corresponding to the first two methods use similar ideas to the corresponding classical projections, but assume that the z-dynamics is describable by wave functions that are products of single particle wave functions in z, each with some z_{opt} for its central positions and having widths that depend upon the location of $\Psi_\perp$. This approach treats the dynamics perpendicular to the surface with a SCP approximation having (nearly) flat (constant frequency) phonon modes polarized perpendicular to the surface and uncoupled to the in-plane phonon modes.[5] The parameters that define the corresponding positional Gaussian distributions are determined from the minimization of the contribution they make to the total energy (at zero temperature) or the free energy (at finite temperature) of the system. The potential energy terms in Eqs. (5) are replaced by the corresponding averages of these potential energies over the corresponding $\Psi_\perp$ Gaussians. The z-positions and widths of these Gaussians are determined self-consistently, in the spirit of standard SCP calculations, as described and implemented in Ref. [10]. Thus the quantum treatment of the energies in Eqs. (5) involved the average over both z and $\boldsymbol{r}$ coordinates of these terms as described in Ref. [10].

V. BINDING ENERGIES AND HEATS OF ADSORPTION

Connecting the heats of adsorption to the binding energy of a adatom to a given substrate requires a model for the thermodynamics of the monolayer. Here we use two rather simple but quite adequate models. The connection being used between the isosteric heat of adsorption q_{st} and the theoretical binding energy ϵ_0 is either:

$$q_{st} = \frac{3}{2}kT + \epsilon_0 \tag{7a}$$

or

$$q_{st} = \frac{5}{2}kT + \epsilon_0 \tag{7b}$$

where T is the absolute temperature. The first equation is obtained by using the standard connection between q_{st} and the chemical potentials of both 2D and 3D ideal gases (see Ref. [9], page 251 and Ref. [11], page 157). For this model, the assumption is that the energy consists of the binding energy of the adatom to a flat surface plus the kinetic energy contribution from an ideal, classical 2D gas. Thus, the binding energy ϵ_0 is just $-E_z$, the negative of the energy associated with the z-coordinate using only the U_0 term. Proper inclusion of the effects of the corrugation should increase the binding energy and isosteric heat estimates. The second equation is that of a 3D ideal gas in contact with 2D lattice gas of 3D oscillators placed on random surface adsorption sites. Here, ϵ_0 is the SCP energy of isolated, 3D Einstein oscillators subjected to the full BR model interaction (but no xenon-xenon interactions).[5,10] For this model, the binding energy includes contributions from all three energy terms: E_z, E_{xy}, and E_{xyz}. These are calculated using a SCP treatment of N identical, isolated, anisotropic, 3D Einstein oscillators. For both theoretical models, the inclusion of the mutual interaction between the xenon adatoms should increase both ϵ_0 and q_{st}. While these are simple physical models, they should give acceptable estimates of the monolayer thermodynamics.

VI. XENON RMS VIBRATIONAL AMPLITUDES

One approach to the determination of the corrugation that was explored is the calculation of the RMS amplitude of the in-plane vibration of the $\sqrt{3}$ phase. This value has been determined experimentally,[12] and can easily be calculated from theoretical models. The calculation based upon the MD simulation uses the same analysis as a calculation of the diffusion constant, mainly calculating the average (over t_0 and all atoms) for the mean squared displacement:

$$\langle (\boldsymbol{r}(t_0+\delta t) - \boldsymbol{r}(t_0)) \cdot (\boldsymbol{r}(t_0+\delta t) - \boldsymbol{r}(t_0)) \rangle \,, \tag{8}$$

and examining this expression as a function of the time shift δt. If this expression saturates as a function of δt, then there is no diffusion and the saturation value (obtained by an average over δt for large δt values) is related to the RMS vibrational amplitude. In particular, if $\delta\boldsymbol{r}$ is the 2D displacement from the equilibrium point and the dynamics of $\boldsymbol{r}$ is that of a 2D isotropic oscillator with random initial positions, expression (8) is equal to $2\langle \delta\boldsymbol{r} \cdot \delta\boldsymbol{r} \rangle$, or four times the square of the RMS amplitude of vibration However, if there is diffusion, then the quantity in expression (8) has a asymptotic linear dependence on δt with a slope that is proportional to the diffusion constant.

For the BR:64K case study, diffusion is absent for $T \leq 101$ K. However, for the U25-H:20K case study, diffusion starts to be a problem at a temperature $T \approx 50$ K, and thus the estimated RMS amplitude near that temperature is suspect. Unfortunately, in this system, both the MD and the SCP[5] results indicate that the in-plane

TABLE I. Parallel and perpendicular RMS amplitudes of vibration for $\sqrt{3}$ xenon on the Pt surface. The temperatures T are in kelvin and the vibrational amplitudes are in Å.

Source	T	Parallel	Perpendicular
Diehl[a]	80	0.23	0.17
	110	0.35	0.17
MD[b]	29	0.17	—
	46	0.21	—
	88	0.29	—
	101	0.31	—
MD[c]	33	0.20	—
	52	0.25	—
Q2D[d]	80	0.25	0.13
	110	0.29	0.16

[a] Experiment: See Ref. [12].
[b] This work: Case study BR:64K.
[c] This work: Case study U25-H:20K.
[d] SCP theory using the full BR model as in Refs. [5 and 10].

RMS amplitude is relatively insensitive to the corrugation. Given that this RMS amplitude was difficult to determine with high precision in the LEED experiment,[12] it was not possible to use this approach to narrow the range of possible values for the corrugation. The experimental and theoretical values are listed in Table I, and the agreement is within the experimental uncertainty. We interpret the MD and SCP results to be an indication that the in-plane vibrational amplitude is dominated more by the xenon-xenon interaction and less by the surface corrugation. The theoretical perpendicular values are calculated by the quantum approach described in the main article.

VII. EFFECTS OF PLATINUM DYNAMICS

The main article discusses mechanisms that could reduce the corrugation beyond that found with the projection models presented here. One such mechanism is the thermal motion of the platinum surface, which would reasonably be expected to be more important at higher temperatures since higher temperatures would imply larger amplitude oscillations of the surface. A very simple estimate of the order of magnitude of such an effect can be made by estimating the size of the surface normal motion of the platinum and using that to estimate the possible variation in the corrugation. The surface modes of platinum with a xenon monolayer have been examined, and these modes show a strong, sharp peak in the platinum response (associated with the surface normal motion) at a frequency such that $\hbar\omega = 185.6$ K.[13] If this is used in a simple model, the one-dimensional SHO, then the RMS deviation in the z-position of the platinum surface is given by the equation:

$$\delta z_{rms}^2 = \frac{\hbar}{2M\omega}\coth(0.5\beta\hbar\omega) \qquad (9)$$

where M is the platinum atomic mass, β is the inverse temperature, and ω is the platinum response frequency. For a temperature of 10 kelvin, this estimate gives $\delta z_{rms} = 0.026$ Å while at 120 kelvin it gives 0.032 Å. For comparison, the shift in z_{opt} as the xenon atom moves laterally over the platinum surface barrier is about 0.10 Å, larger but not orders-of-magnitude larger than the δz_{rms} at $T = 120$ K. Perhaps more relevant, the increase in the z_{opt} for a xenon adatom at the Atop site, as the temperature is raised from 0 to 100 K, is about 0.05 Å, and this produces a 20 % decrease in the effective corrugation of the surface. Finally, simply recalculating the $U_{\boldsymbol{G}}$ after increasing z_{opt} by 0.04 Å reduces the corrugation by about 7 %. While the δz_{opt} shift is small, its effects might not be completely negligible at the transition temperature as judged by comparison to other smoothing effects. Furthermore, motion of the Pt surface could prevent the xenon atoms from maintaining the optimal z-distance from that surface, thus further reducing the effective corrugation. It is not unreasonable to expect further smoothing of the corrugation due to this effect, but how much is not possible to determine without examining the dynamical coupling between the adlayer and the substrate. A robust argument can be made that this dynamical coupling could play an important role in determining the melting temperature,[14] but this needs more investigation using both theory and experiment.

VIII. ADDITIONAL RESULTS AND DISCUSSION

Below about 60 K, different initializations did produce different final results, often generating distinctly different structures and causing small shifts in the thermodynamic functions. However, these low temperature runs appear to merge (as they were heated above approximately 60 K) into a common set of thermodynamic values with similar (although not identical) structures. The exact temperature at which this happens does vary from case study to case study. Cooling from a state of uniform gas produced the same hysteresis as found in Ref. [3].

A. Constrained Geometry

Results for system sizes 64K, 16K, and 4K show essentially the same total energies at corresponding temperatures. The differences (which are of the order of 0.1 kelvin) are well within the statistical noise. The same is true for ψ_6, with any variation due to system size being within the noise of the data as shown in Fig. 2.

The drop in ψ_0 as the transition is approached from below, as seen in Fig. 3, is far sharper than that for ψ_6. This is consistent with ψ_0 likely being the more appropriate order parameter to describe this order-disorder transition.[2] Furthermore, ψ_0 does show a variation with system size in the tail of the curve just above the transition, as illustrated by Fig. 3. Postulating that ψ_0 is the appropriate

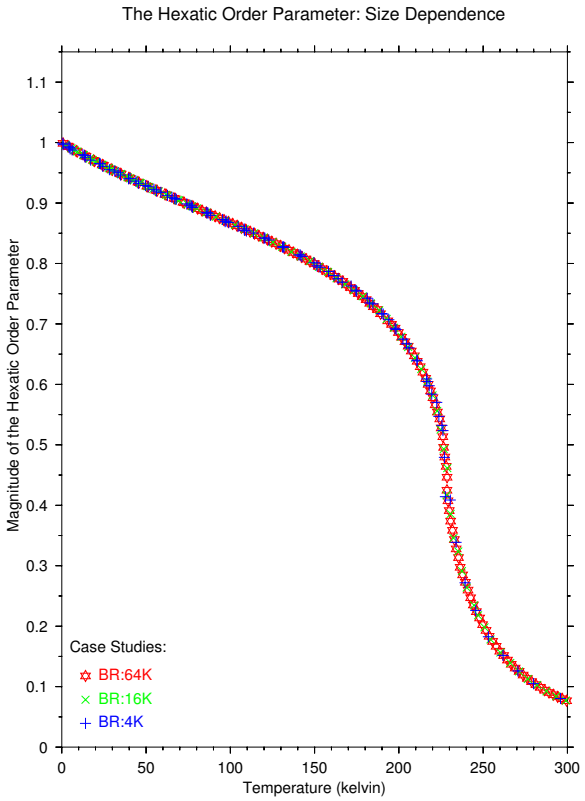

FIG. 2. The hexatic order parameter of three case studies, illustrating the size dependence for constrained geometries.

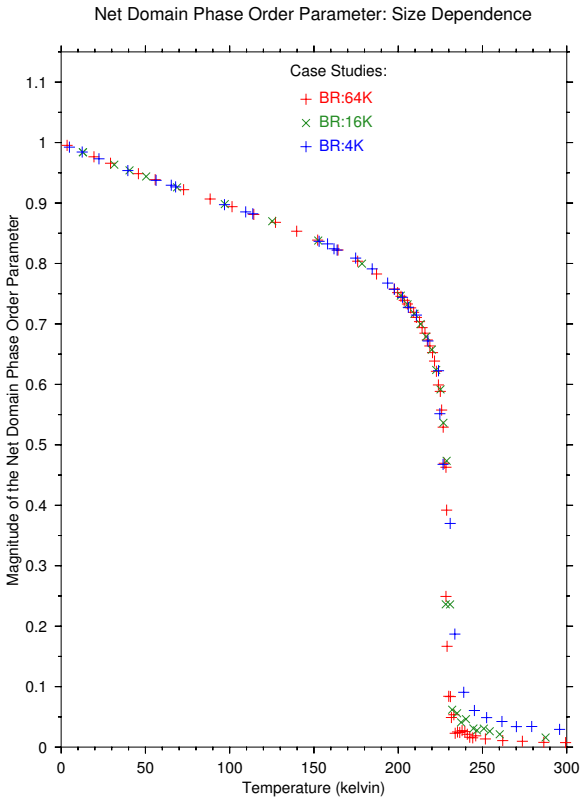

FIG. 3. The NDP order parameter ψ_0 of three case studies, illustrating the size dependence for constrained geometries. The initialization is the $\sqrt{3}$ phase for all.

order parameter for this system, this sensitivity is to be expected.[2] The insensitivity of ψ_6 to system size, and its more gradual drop to zero with increasing temperature, implies that it is not likely the most appropriate order parameter for this transition.[2]

An examination of the ground state of the constrained geometry was carried out for the BR projection because it has the more appropriate corrugation for very low temperatures. The classical ground-state energy is obtained by an extrapolation of the finite temperature total energy to zero temperature.[4] As an example, comparisons for the BR projection using a system size of 64K and initial states of the $\sqrt{3}$, AIC, and SIC structures, show that the stable, zero pressure ground state is the $\sqrt{3}$ phase. Figure 4 shows a plot of the ground-state energy of the AIC and SIC phases as a function of inverse density. It is clear that the $\sqrt{3}$ structure is the stable zero pressure phase. At finite misfits, the AIC phase is decidedly preferred to the SIC phase except for small misfits (having scaled densities > 1.00 but < 1.003). For these small misfits, the difference in energy between the AIC state and the SIC state is zero within statistical uncertainty. It is reasonable to assume that these small differences between the energies of the AIC and SIC phases could be an important driver for the "chaotic" behavior of the domain structure that is observed in this system. Similar results are found in the unconstrained case studies as shown in Sec. VIII B below.

Preliminary calculations of quantum effects (using a

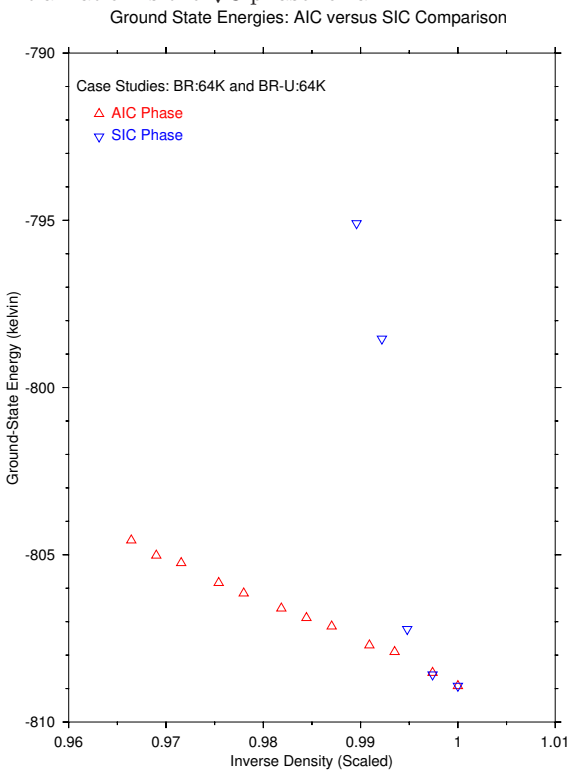

FIG. 4. Ground state energy for constrained simulations, comparing the AIC phase (case study BR:64K) and the SIC phase (case study BR-U:64K). The density is scaled to that of the $\sqrt{3}$ phase.

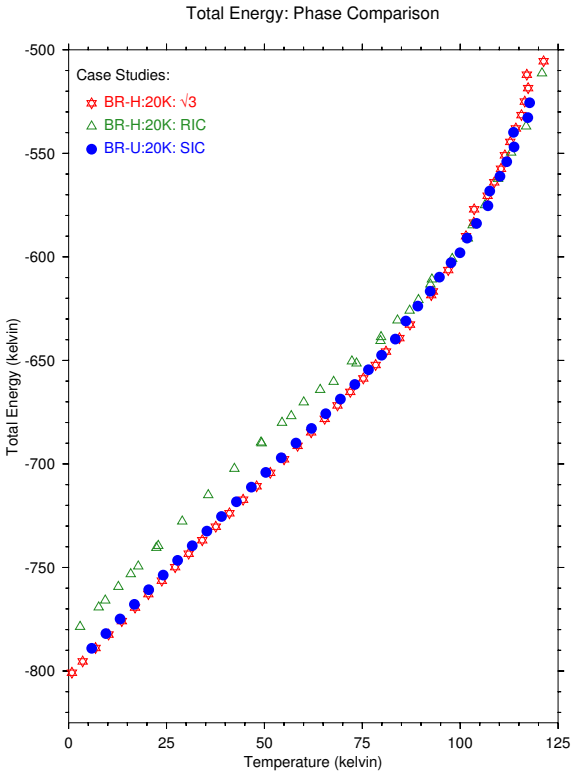

FIG. 5. The total energy of the case studies for BR-X:20K, comparing initializations in the $\sqrt{3}$, RIC, and SIC initial states for the unconstrained geometry. They all have essentially the same average density of $0.5\rho_0$, and only the heating data is shown.

SCP approach for large clusters) indicate that these conclusions are not substantially altered by such effects and that the basic behavior described here also holds for low temperatures when quantum effects are included.[15] The preliminary calculations show free energy curves that look much like the energy curves in Fig. 4.

B. Unconstrained Geometry

The initialized structures appear to be, after some initial relaxation into a quiescent state, quite stable. However, different initializations often stabilized with different structures and even different energies existing at the same system temperature. This is taken to be an indication that the system settles into meta-stable states which have long lifetimes on the scale of the MD simulation. Since the stable state at finite temperature is determined by the lowest free energy, the arguments in Sec. III are used to determine the most likely stable state at finite temperatures.

Figure 5 compares the total energy of unconstrained $\sqrt{3}$ and corresponding meta-stable RIC and SIC initializations for the BR-X:20K case study. The $\sqrt{3}$ initialization shown starts with a hexagonal patch having a single domain and minor imperfections on the boundary of the patch. The RIC initialization starts with a hexagonal patch of the $\sqrt{3}$ initialization, but then rotates it by 2° counterclockwise before starting the simulation. The SIC initialization shown starts with a rectangular patch having almost equal sides and 8 stripes (which are roughly parallel to the $[1,1]$ direction of the xenon lattice). It can be seen that the $\sqrt{3}$ points are lower in energy than either of the IC data sets. However, note the closeness of the SIC and the $\sqrt{3}$ data sets, even though the SIC structure was initialized with the maximum number of stripes possible (8) without mechanical instabilities causing the simulation to abort.

At some temperature below 100 K, the three separate data point sets merge into a single set of points exhibiting a $\sqrt{3}$ like structure, thus presumably satisfying the conditions set forth in Sec. III. Using the free energy analysis of that section, it appears that the $\sqrt{3}$ phase is, in this temperature range, the most stable state of the three. However, the SIC phase is very close to the $\sqrt{3}$ phase in (free) energy, implying that the SIC can easily compete with the $\sqrt{3}$ phase. The MD results do imply that not only is the $\sqrt{3}$ phase the ground state of this system, it is always stable against both the RIC and SIC phases until it disorders (melts).[2] The existence of a stable $\sqrt{3}$ phase up to the disordering (melting) transition also occurs for corrugations more appropriate to the higher temperatures in this figure. However, the temperature of the transition from the chaotic state to the $\sqrt{3}$ phase does depend upon the value of the corrugation.[2]

Stability comparisons between different initializations were carried out only for the heating-cycle data set because the cooling-cycle data exhibits hysteresis if the system is cooled from a disordered state. For example, consider a $\sqrt{3}$ initialization started at a very low temperature, then slowly heated past the transition to the disordered state, then cooled down to very low temperatures (close to the initial temperature). Figure 6 demonstrates this hysteresis in the case study BR-H:20K, showing the hysteresis effects of heating and cooling in the simulations. The upper (cooling cycle) branch, which is unstable to the lower (heating cycle) one, is associated with a collection of small patches of $\sqrt{3}$ structures instead of the one large patch found in the lower branch.

In the heating process, most runs were carried out to 16.3 ns, the averages then taken over the last 3.26 ns. For a select set of temperatures, the runs were carried out to 35.9 ns, and the averages again taken over the last 3.26 ns. Note that the longer runs shown in Fig. 6 are the ones slightly to the left of the main heating data set, showing that some relaxation is still present in the transition from order to disorder. The cooling data set does not retrace the heating data set, the low temperature state (upon cooling) being a meta-stable structure with "islands" of registered structures with about 100–300 atoms per island.[2] Using the arguments of Sec. III, it is clear that the lower data set is the more stable branch and the upper branch is less so. This is consistent with the usual arguments used at very low temperatures where the energy term dominates the free energy.

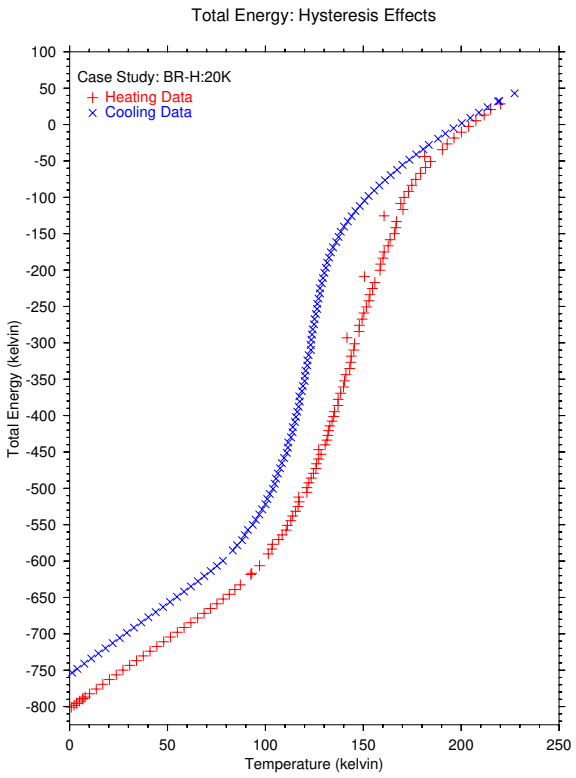

FIG. 6. The total energy for case study BR-H:20K using the $\sqrt{3}$ initialization. Both heating-cycle data (lower curve) and cooling-cycle data (upper curve) are shown. Data points off the curve for the heating cycle data show the effects of averaging over the time interval $[32.6, 35.9]$ ns instead of the usual $[13.0, 16.3]$ ns.

Assuming the validity of the BR Model, either the BR projection (strictly classical) or the U30 projection (quantum corrections) would be the appropriate corrugation for very low temperatures. Nevertheless, simulations were carried out for other corrugations at these low temperatures in order to test the stability of the $\sqrt{3}$ ground state to variations in the corrugation. For $U_{(10)}$ values of -25, -20, and -15 kelvin, all MD simulations show the IC structure to be the ground state of the system, but still having a stable $\sqrt{3}$ structure at higher temperatures (but still below melting). If the corrugation is lowered much below $U_{(10)} = -15$ K, there is no stable $\sqrt{3}$ phase at any temperature, the exact value at which this occurs not being examined here.

The MD specific heat shows no clear sign of a transition near 60 K. If the system is initialized in the $\sqrt{3}$ structure at low temperature, the ψ_0 order parameter decreases monotonically with increasing temperature, showing smooth behavior from low temperatures to melting. The system stays in the $\sqrt{3}$ phase until the disordering temperature is reached. However, if the system is initialized in an IC structure at low temperature (thus having a small ψ_0 value), above 60 K there is an increase in ψ_0 with temperature.[2] Some experimental papers[16] claim a transition from a low temperature striped phase to the $\sqrt{3}$ phase as the temperature is raised above 60 K. For all the corrugations and initializations investigated here, the simulations show a gradual transition from the initial low temperature structure into the $\sqrt{3}$ phase at higher temperatures, but the temperature range of this transition does depend upon both the corrugation and the initialization. The transition does not seem to be a true thermodynamic transition, but rather appears to be a gradual evolution into the $\sqrt{3}$ structure. However, this apparent behavior could be a consequence of the very long relaxation times for this system and not a reflection of the system's true equilibrium thermodynamics.

C. Structure of the Monolayer

Our simulation shows there is no tendency for the submonolayer patch to spontaneously rotate away from the high symmetry direction of the substrate. This behavior is in contrast to that of Xe/Gr,[3] and it is probably due to Xe/Pt having a much stronger corrugation and a dilated lattice compared to Xe/Gr. Even when the issue is forced by the generation of a rotation in the initial state, the imaginary part of ψ_6 quickly becomes very small (about 10^{-2} once the system has stabilized) thus indicating a near zero rotation angle.[3] A small initial rotation angle generates rather irregular domain shapes, the typical size of these domains being dependent upon that angle. However, unlike the Xe/Gr case where the whole patch rotates to the stable angle,[3] the edges of these Xe/Pt patches remained (approximately) at the original rotated orientation with respect to the substrate. The adatoms in the domains simply re-position themselves to produce local alignment with the $\sqrt{3}$ state orientation, and the domain walls respond (relax) accordingly, forming a chaotic, meta-stable structure.

Initial structures generated by small initial rotations result in large domains of the $\sqrt{3}$ structure separated by narrow walls (generally zero to 2 atoms wide) that run in a irregular manner through the system. Those generated by large rotation angles tend to have smaller domains possessing more regular boundaries. Using the analysis outlined in Sec. III, these various structures are found to be thermodynamically unstable to the $\sqrt{3}$ state.

Initializations generated by small increases in the initial density tend to have larger domains with domain walls that tend to be straighter but otherwise similar to the walls in the initializations generated by a rotation. The range of interior patch densities that can be used to initialize an unconstrained geometry without the system becoming mechanically unstable is quite small. While there is no simple and reliable way to estimate the patch density, the densest initialization had about 6 % of the atoms in irregular, super-heavy-like domain walls with the others in the three types of domains[3] having domain populations of roughly 25 to 50 %. Attempts to initialize with higher patch densities result in simulations aborting with loss of energy conservation. As stated previously, the $\sqrt{3}$ patch is the thermodynamically stable state, but

the others can be thermodynamically meta-stable, often without any major reconstructions over 16.3 ns or longer. Only selected runs were tested beyond this, but they too were meta-stable.

The initial relaxation of the system often results in domains of various geometries without a clear pattern. When the simulation was allowed to evolve at fixed energy, the walls seem to be pinned down and rather resistant to movement. This is true even when thermodynamic analysis indicates that the state in question is not a stable structure. Rather, these structures do appear to be meta-stable on the time scale of any reasonable MD simulation. We label such structures "chaotic". This is in marked contrast to the behavior of the walls found in the Xe/Gr system, where the domain walls have a regular structure, are relatively wide, and are of essentially constant width.[3,4] Furthermore, the walls in the Xe/Pt system, at least for the unconstrained cases, do not match the description of domain walls used in many, if not most, of the calculations in the literature on this subject.[17–19]

IX. EXISTENCE OF METASTABILITY

Our data shows strong evidence of meta-stability and hysteresis. However, the difficultly of making statements about meta-stability based upon the results of any MD simulation is two-fold. First: The time scale of any practical MD simulation is very small on the scale of macroscopic experiments, the longest run in these simulations corresponding to about 49 ns. Second: The system size of the simulation cell is usually much smaller than the macroscopic system. Although the justification here is a bit sounder, as the largest simulation presented here is comparable to the smaller experimental examples, the size is still smaller than the best experimental cases. Nevertheless, even with those caveats, it is clear that the meta-stability observed here is qualitatively different than that observed for Xe/Gr simulation.[3,4] While it is not possible to make a definitive conclusion, one can still draw the reasonable inference that meta-stability must be considered a strong possibility in this system. This thought is bolstered by the fact that the free energy analysis of the MD results shows that, while the $\sqrt{3}$ phase is the stable phase for the BR model (the unconstrained geometry case) below the disordering temperature, the SIC phase (with a small misfit) is very close in free energy to the $\sqrt{3}$ phase. It is then possible that any lack of thermal equilibrium could drive competition between these (and possibly other) states. In fact, we have observed "chaotic" states which consisted of broad bands of $\sqrt{3}$ domains, which were much longer than they were wide, mixed in with configurations that have a roughly hexagonal shape. Figure 5 in the main text is one such example. These meta-stable structures are interesting, not only in their own right, but because of their relation to the general study of chaotic systems and even, perhaps, to our understanding of the third law of thermodynamics.[20,21]

[1] L. W. Bruch, R. D. Diehl, and J. A. Venables, Rev. Mod. Phys. **79**, 1381 (2007).
[2] A. D. Novaco, L. W. Bruch, and J. Bavaresco, Phys. Rev. B **91**, 161412 (2015).
[3] A. D. Novaco and L. W. Bruch, Phys. Rev. B **89**, 125431 (2014).
[4] L. W. Bruch and A. D. Novaco, Phys. Rev. B **77**, 125435 (2008).
[5] L. W. Bruch and A. D. Novaco, Phys. Rev. B: Condens. Matter And Matt. Phys. **61**, 5786 (2000).
[6] F. Rief, *Fundamentals of Statisitical and Thermal Physics* (McGraw-Hill, New York, 1965).
[7] W. A. Steele, Surf. Sci. **36**, 317 (1973).
[8] W. A. Steele, *The Interaction Of Gases With Solid Surfaces*, vol. 3 of *The International Encyclopedia Of Physical Chemistry And Chemical Physics. Topic 14: Properties Of Interfaces,* (Pergamon Press, Oxford, New York, 1974).
[9] L. W. Bruch, M. W. Cole, and E. Zaremba, *Physical Adsorption*, International Series Of Monographs On Chemistry; No. 33 (Oxford University Press, New York, 1997).
[10] A. D. Novaco, Phys. Rev. B: Condens. Matter **46**, 8178 (1992).
[11] R. Baierlein, *Thermal Physics* (Cambridge University Press, New York, 1999).
[12] R. D. Diehl, T. Seyller, M. Caragiu, G. S. Leatherman, N. Ferralis, K. Pussi, P. Kaukasoina, and M. Lindroos, J. Phys.: Condens. Matter **16**, S2839 (2004).
[13] R. D. Boutchko and L. W. Bruch, Phys. Rev. B **70**, 195422 (2004).
[14] A. D. Novaco and J. P. McTague, Phys. Rev. B: Condens. Matter **20**, 2469 (1979).
[15] A. D. Novaco (unpublished).
[16] K. Kern, Phys. Rev. B **35**, 8265 (1987).
[17] K. Kern, R. David, P. Zeppenfeld, R. Palmer, and G. Comsa, Solid State Commun. **62**, 391 (1987).
[18] E. D. Specht, A. Mak, C. Peters, M. Sutton, R. J. Birgeneau, K. L. D'Amico, D. E. Moncton, S. E. Nagler, and P. M. Horn, Z. Phys. B **69**, 347 (1987).
[19] M. Kardar and A. N. Berker, Phys. Rev. Lett. **48**, 1552 (1982).
[20] L. Masanes and J. Oppenheim, Nat. Commun. **8**, 14538 (2017).
[21] M. Aizenman and E. Lieb, J. Stat. Phys. **24**, 279 (1981).